JAGIELLONIAN UNIVERSITY
IN KRAKOW

FACULTY OF PHYSICS, ASTRONOMY AND APPLIED
COMPUTER SCIENCE

WESTFÄLISCHE
WILHELMS-UNIVERSITÄT
MÜNSTER

INSTITUTE OF PHYSIOLOGY II

Pulse-pressure dependent nanomechanics of vascular endothelium

Jacek Szczerbiński

A MASTER THESIS
WRITTEN UNDER SUPERVISION OF
PROF. MAREK SZYMOŃSKI AND DR. JOHANNES FELS

Kraków, 2013

1556266275(1)

ABSTRACT

Vascular endothelium *in vivo* is constantly exposed to pulse-pressure waves. Concurrently, blood pressure *per se* influences vascular physiology – it elicits dynamic reorganization of the submembraneous actin network, whereas cortical actin dynamics regulates endothelial function, in particular production of nitric oxide (NO). Yet, the nature of pressure sensing in the endothelium remains obscure.

To study the interplay between blood pressure, cortical actin and NO, we developed an experimental setup combining an atomic force microscope (AFM) with a confocal laser scanning microscope (CLSM). The experimental system provided the means to evaluate endothelial nanomechanics dependent on pulse-pressure waves, and to concurrently monitor the structure of the cell and production of NO by means of fluorescence microscopy. Diastolic blood pressure was simulated by application of constant hydrostatic pressure, while the AFM cantilever was used as a local pressure transducer to mimic pulse waves. Hence, quasi-physiological pressure waves (120/80 mmHg or 40/0 mmHg, 60 beats per minute) were applied to the surface of an individual endothelial cell.

Local application of pulsatile pressure (40/0 mmHg) on the surface of an aortic endothelial cell did not evoke a whole-cell reaction, and in particular any increase in NO production. No impact of local pressurization on production of NO resulted either from limited area of stimulation, or from absence of shear stress and circumferential strain. The network of actin stress fibers was locally deformed/ disrupted by quasi-physiological pressure waves. Concurrently, the nucleus was displaced and deformed. Yet, the bulk of the cell sustained its initial shape, and the local deformation of the cytoskeleton did not evoke a reaction of the entire cell. Most trials were performed at 40/0 mmHg, but the effects of pressurization with 120/80 mmHg was not significantly different.

This novel approach enables, for the first time, the investigation of cortical nanodynamics in pressurized vascular endothelium. The versatile setup may be modified to exert global physiological hydrostatic pressure on endothelial cells. Hence, the effects of local and global pressurization could be compared, yielding valuable information on pressure sensing by the endothelium. Shear stress may be introduced into the setup and is expected to amplify the effect of pulse pressurization on endothelial cells. Further studies are bound to shed light on the pressure dependent physiology of the endothelium *in vivo*.

Tytuł pracy

Wpływ ciśnienia tętniczego na nanomechanikę komórek śródbłonka naczyniowego

Streszczenie

Śródbłonek naczyniowy *in vivo* nieustannie poddawany jest działaniu ciśnienia tętniczego. Ciśnienie krwi wpływa na fizjologię układu krwionośnego, powodując m. in. reorganizację cytoszkieletu komórek śródbłonka. Jednocześnie aktyna zlokalizowana w części kortykalnej cytoszkieletu reguluje funkcjonowanie śródbłonka, w szczególności produkcję tlenku azotu (NO). Pomimo rozwoju badań w zakresie fizjologii układu krwionośnego, mechanizm reakcji śródbłonka na przyłożenie ciśnienia nie został jak dotąd wyjaśniony.

Aby efektywnie badać zależności między ciśnieniem krwi, korową warstwą cytoszkieletu i produkcją NO, w ramach przeprowadzonych badań opracowano układ doświadczalny oparty na mikroskopie sił atomowych (AFM) i skaningowym mikroskopie konfokalnym (CLSM). Układ ten pozwala na badanie właściwości mechanicznych śródbłonka, poddanego działaniu quasi-fizjologicznego ciśnienia tętniczego. Jednocześnie, możliwe jest monitorowanie struktury komórki i syntezy NO przy pomocy mikroskopii fluorescencyjnej. Przyłożone stałe ciśnienie hydrostatyczne odpowiada rozkurczowemu ciśnieniu krwi, zaś periodyczne fale ciśnienia skurczowego są aplikowane poprzez naciskanie komórki próbnikiem AFM. W ten sposób pojedyncza komórka śródbłonka poddawana jest quasi-fizjologicznym falom ciśnienia tętniczego (120/80 mmHg lub 40/0 mmHg, 60 impulsów na minutę).

Lokalne przyłożenie periodycznego ciśnienia (40/0 mmHg) do powierzchni komórki śródbłonka aorty nie wywołuje całościowej odpowiedzi komórki, w szczególności wzrostu produkcji NO. Brak wpływu lokalnej aplikacji ciśnienia na syntezę NO wynika z ograniczonej powierzchni poddanej stymulacji, bądź z braku ciśnienia przepływu krwi oraz obwodowego ciśnienia tętniczego. Struktura aktynowych włókien naprężeniowych zostaje miejscowo odkształcona lub przerwana poprzez mechaniczną stymulację próbnikiem AFM. Jednocześnie, jądro komórkowe ulega przesunięciu bądź odkształceniu. Tym niemniej, komórka zachowuje swój pierwotny kształt, a miejscowe odkształcenie cytoszkieletu nie wywołuje odpowiedzi całej komórki. Otrzymane wyniki uzyskane dla ciśnień 120/80 mmHg i 40/0 mmHg jakościowo są podobne.

Opracowana nowatorska metoda pomiarowa umożliwia badanie nanodynamiki kortykalnej warstwy cytoszkieletu aktynowego w komórkach śródbłonka poddanych działaniu ciśnienia tętniczego. Zaprojektowany układ jest uniwersalny – można go wykorzystać do przyłożenia ciśnienia tętniczego na całej powierzchni komórki, umożliwiając tym samym porównanie efektu lokalnej i globalnej stymulacji śródbłonka ciśnieniem. Taki eksperyment może udzielić istotnych informacji nt. mechanizmu „odczuwania" ciśnienia przez śródbłonek. Opracowany układ umożliwia również stymulację śródbłonka ciśnieniem przepływu krwi, co prawdopodobnie wzmocni efekt indukowany w komórkach ciśnieniem tętniczym. Dalsze badania w tym kierunku pozwolą na dokładne poznanie fizjologii śródbłonka poddanemu ciśnieniu *in vivo*.

Abbreviations used in the thesis

AFM – atomic force microscopy/ microscope

CLSM – confocal laser scanning microscopy/ microscope

DAF-FM - diaminofluorescein-FM (F – fluorine, M – methyl)

eGFP – enhanced green fluorescent protein

eNOS – endothelial nitric oxide synthase

NO – nitric oxide

TABLE OF CONTENTS

1 INTRODUCTION 7

1.1 Pressure acting on the endothelium 7

1.2 Pulse pressure 8

1.3 Cytoskeletal actin, its dynamics and release of nitric oxide 10

2 MATERIALS AND METHODS 12

2.1 Pressurization of endothelial cells 12

2.1.1 Pressurization with 40/0 mmHg 12

2.1.2 Pressurization with 120/80 mmHg 13

2.1.3 Shape of the pulse 15

2.2 Control of exerted pressure 16

2.3 Measurement of elasticity – nanoindentation spectroscopy 19

2.4 Fluorescence microscopy 21

2.4.1 Lifeact staining of actin filaments 22

2.4.2 Hoechst staining of nucleus 24

2.4.3 DAF-FM staining of nitric oxide 25

2.5 Artifacts and experimental difficulties 26

2.5.1 Drift of the substrate 26

2.5.2 AFM laser interference 29

2.5.3 Excitation of the cantilever by the scanning laser beam 31

2.5.4 Autofluorescence of the AFM probe 32

2.6 Processing of force-distance curves 33

2.7 Experimental 34

2.7.1 Atomic force microscopy 34

2.7.2 Conditions of measurements 35

2.7.3 Cell culture 35

2.7.4 Fluorescence microscopy 35

2.7.5 Cell staining 36

3 RESULTS 37

3.1 Height and elasticity of the pressurized region 38

3.2 Displacement of the nucleus 39

3.3 Deformation of actin cytoskeletal fibers 40

3.4 Deformation of the bulk 44

3.5 Production of NO 46
3.6 Cells pressurized over the nucleus 48
3.7 Experiments with 120/80 mmHg pulse pressure 49
3.8 Experiments without control of the substrate drift 52
4 CONCLUSIONS 54
4.1 Physiological findings 54
4.2 Technical solutions 57
5 PROTOCOLS 59
5.1 Collagen matrix 59
5.2 HEPES buffer 60
5.3 Cell culture medium 60
5.4 Cell culture routine 61
5.5 Lifeact transfection 61
5.6 Hoechst staining 62
5.7 DAF-FM staining 62
6 BIBLIOGRAPHY 64

1 INTRODUCTION

The reported experiment consists of smart application of sensitive mechanical and optical methods for studying physiological phenomena on the level of a single cell. This section describes the key concepts of physiology and molecular biology explored in the study.

We start with a brief description of mechanical forces acting on the endothelium *in vivo* (section 1.1). Then we explain the nature of pulse pressure (section 1.2) – the component of hemodynamic stress whose impact on endothelial physiology has been reported in the literature, but not yet explained. In the reported experiment, pulse pressure was applied locally to the surface of a single endothelial cell, expecting to elicit a response of the cell in terms of cortical actin nanodynamics and production of nitric oxide. Hence, section 1.3 deals with cytoskeletal actin and explains the role of nitric oxide in vascular physiology.

1.1 Pressure acting on the endothelium

The endothelium, being the innermost layer of blood vessels, is constantly exposed to mechanical stress exerted by blood. Three types of hemodynamic forces are identified [1] (Figure 1.1):

- shear stress – exerted by the blood flow,
- circumferential strain – cyclic stretch, due to vessel deformation,
- hydrostatic pressure – periodic load applied normal to the cell surface, due to blood pressure.

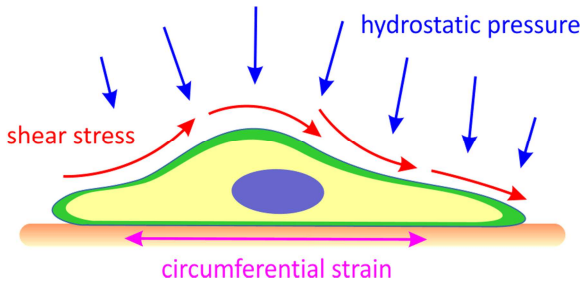

Figure 1.1. Three kinds of hemodynamic forces acting on the endothelium *in vivo*. All of them contribute to proper functioning of endothelial cells. The effect of shear stress and circumferential strain on the endothelial physiology has been widely studied, yet hydrostatic pressure has been generally unappreciated in the literature.

Ideally, endothelial cells should be cultured and examined in presence of all the mentioned forces, so that the conditions are as close as possible to *in vivo* environment. Absence of any of the three stress components results in a deviation from normal endothelial function, manifested in decreased

production of nitric oxide (NO) [2]. In practice, endothelial cells are usually cultured under atmospheric pressure, disregarding the tonic mechanical stress present in blood vessels.

The effect of shear stress and circumferential strain on endothelial physiology has been widely investigated. Considerable attention has been devoted to the dynamic mechanical stress, revealing its ability to regulate shape and arrangement of the cells [3], and even to discriminate between arterial and venous endothelium [4]. Concurrently, few studies have focused on hydrostatic pressure and its impact on endothelial function. There is evidence for changes in phenotype and cytoskeletal architecture of endothelial cells exposed to chronic high pressure [5,6], and a number of studies have dealt with proliferation of endothelium subjected to elevated hydrostatic pressure [5], yet few experiments have dealt with pulse pressure. The pioneering work by Casey et al. [2] demonstrated the importance of pulse pressure for proper endothelial function, but the mechanism of this interplay remains obscure.

1.2 Pulse pressure

The heart works as a pump, forcing blood circulation by repetitive contraction of the left ventricle. Blood ejects the heart and is accommodated in the aorta and arteries, whose walls expand upon receiving a huge amount of fluid. The recoil of smooth muscle surrounding the vessels causes a driving force for the movement of the blood. Thus, a pressure wave emerges and propagates along the arteries, which constitute a waveguide.

Pulse pressure is a measure of the strength of the pressure wave, and is defined as the difference between systolic pressure and diastolic pressure [7]. In the following chapters we shall use the term *pulse pressure* in a broader sense: any periodic hydrostatic pressure varying between 0 and a certain peak value will be called *pulse pressure*. The peak value will be referred to as *pulse pressure amplitude*, and the rate of pressure changes will be called *pulse pressure frequency*. The term *pulse pressurization* shall mean application of pulse pressure to the surface of a cell.

Pulse pressure amplitude is highest in the aorta, and decreases with distance along the arteries, vanishing in the capillaries (Figure 1.2). In the presented study, we investigated the effect of pulse pressure on bovine aortic endothelial cells, hence the applied pressure amplitude was $\sim$ 40 mmHg, which is traditionally perceived as the normal value of pulse pressure amplitude in healthy humans.

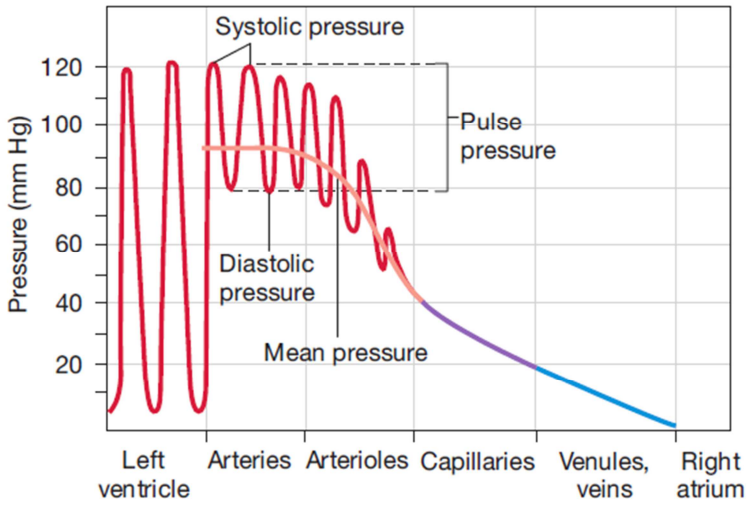

Figure 1.2. The amplitude of pulse pressure throughout the systemic circulation. In the reported study, bovine aortic cells were subjected to pulse pressure. Therefore, an amplitude of ~ 40 mmHg was used, to simulate the physiological pressure waves. Figure reproduced from the literature [7].

Hypertension occurs when systolic and diastolic pressure are consistently over 140 mmHg and 90 mmHg at rest, respectively. Hypertension, being a major cardiovascular risk factor, causes endothelial dysfunction in peripheral, coronary and renal circulation [8]. Concurrently, impaired production of NO by the endothelium is suspected to predispose to the development of essential hypertension [9]. Elevated pulse pressure amplitude itself is a marker of cardiovascular risk, mainly for myocardial infarction [10], and is an independent risk factor for cardiovascular morbidity and mortality [11].

Considering the crucial importance of hydrostatic pressure to development of cardiovascular disease, one may be surprised with the lack of interest of researchers in the effect of hydrostatic pressure (and pulse pressure) on endothelial function. To the best knowledge of the author, the presented study is the first ever approach to investigate the physiological response of the endothelium to pulse pressure on the level of a single cell. Further studies may concern hypertensive pressure and other pathophysiological states, yet the reported experiment focuses on the reaction of endothelial cells to normal blood pressure.

As mentioned above, the endothelium feels and responds to changes in pulse pressure *in vivo*. This implies the existence of an endothelial pressure sensor. The identity of the sensor, or the mechanism underlying the endothelial response to pressure, remains unknown – yet of crucial importance for cardiovascular physiology. The pressure-dependent myogenic response of vascular smooth muscle is essentially independent of the endothelium [12]. Pressure-sensitive ion channels were found in *Escherichia coli* [13], but the question of their existence and potential role in the

endothelium remains open. In the reported study, we applied pulse pressure only to a part of the cell's surface, and watched if any molecular switch triggers a reaction of the cell to pressurization.

1.3 Cytoskeletal actin, its dynamics and release of nitric oxide

The cytoskeleton organizes the cell in space and is responsible for its mechanical interactions with the environment. Those functions are executed by a versatile, dynamic network of fibers (actin filaments, microtubules, and intermediate filaments), moderated by motor proteins (mainly myosins and dyneins). In this study, we shall focus on actin, which concentrates in the cell cortex – the submembraneous layer of dense filamental network supporting the cell membrane, with thickness up to 150 nm.

The dynamics (expression and polymerization/ depolymerization) of cortical actin regulates the activity of endothelial nitric oxide synthase (eNOS) [14,15], which is located just under the cell membrane, at a nanometer distance from the cortical network of filamental actin [16]. eNOS produces the vasodilator NO, which is then released by endothelial cells and induces dilation of blood vessels [17], by relaxation of the aortic vascular smooth muscle. Thus, release of nitric oxide may substantially increase the velocity of blood flow, and so reduce blood pressure. The drop of pressure is restricted by a negative feedback mechanism, called baroreceptor reflex. Yet, it has been reported that after inhibition of autonomic baroreflex mechanisms, nitric oxide tonically restrains blood pressure by approximately 30 mmHg [18]. Hence, production rate of nitric oxide is a key parameter of endothelial function.

The functional state of the cell cortex may be assessed by measuring its elasticity, *e.g.* by using nanoindentation with an AFM probe, or by imaging the actin filaments by means of fluorescence microscopy. Stiffness of the cell cortex anti-correlates with NO production rate, in other words eNOS located next to highly polymerized actin network produces less NO than eNOS laying over depolymerized cortex [14,19].

Cortical actin is organized in a dense network of individual filaments. This layer is supported by a scaffold of thick actin bundles, called stress fibers, prevalent in endothelial cells. Stress fibers effectively transmit forces and regulate cell adhesion to extra cellular matrix, and cell migration, due to mechanical anchoring to focal adhesions [20]. Depending on their function, at least four types of stress fibers are distinguished: dorsal and ventral stress fibers, transverse arcs and the perinuclear actin cap. Dorsal stress fibers are attached to focal adhesions at the distal ends of the fiber. They cannot contract, but they constitute a support for other filaments. The perinuclear actin cap consists of bundles of filaments laying over the nucleus, and maintaining its shape in the interphase. In the

reported experiment, we disrupt dorsal stress fibers and induce deformation of the perinuclear actin cap. Damage of those structures exposes the rest of the cytoskeleton and the nucleus to dramatic deformations.

2 MATERIALS AND METHODS

In the conducted experiment, a selected endothelial cell was subjected to pulse pressure exerted by a probe attached to an AFM cantilever. The effects of the pressurization on the structure and function of the stimulated cell were assessed in terms of:

- elasticity of the cell cortex,
- height of the pressurized area,
- arrangement of the cytoskeletal actin fibers,
- deformation of the bulk,
- displacement of the nucleus,
- production of nitric oxide.

In order to evaluate those features, we used nanoindentation spectroscopy and confocal laser scanning microscopy. These two techniques could not be used exactly simultaneously (see section 2.5.4), but they were applied alternately: the cell was pressurized and monitored with the AFM for 5-10 minutes, and then imaged with the CLSM for 0.25-2.5 minutes. This sequence was executed repetitively for a period of ca. 2.5 hours.

2.1 Pressurization of endothelial cells

Blood pressure varies between 120 and 80 mmHg. However, for technical reasons (described further in section 2.5.1), most experiments were conducted under ambient pressure, that is with pressure varying between 40 and 0 mmHg. Additional trials were performed for the 120/80 mmHg variant.

2.1.1 Pressurization with 40/0 mmHg

Periodic pulse pressure was transduced to the surface of an endothelial cell, utilizing an AFM setup (Figure 2.1) equipped with a spherical probe of a large diameter, capable of exerting controlled pressure over a region on cell surface. The probe was indented into the cell and retracted to equilibrium position once per second, to mimic the pulse rate of 60 beats per minute. The exerted pressure is quantified in section 2.2. The trials were conducted in BioCell fluid cell, delivered by JPK Instruments.

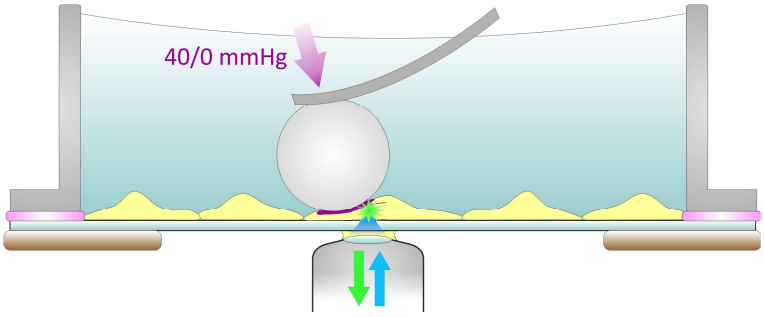

Figure 2.1. The AFM setup utilized for local pressurization of an endothelial cell with periodic pressure varying between 40 mmHg and atmospheric pressure. A spherical probe attached to an AFM cantilever was repetitively indented into the cell's surface, mimicking pulse pressure. The pressurized area is marked in purple. The fluid cell was heated on the sides, to maintain the temperature 37 °C. Concurrently, fluorescence images were acquired using an inverted confocal laser scanning microscope, equipped with an oil immersion objective. The brown pads are the support of the coverslip mounted in the BioCell, and the pink seal is a rubber part, preventing leaks from the fluid cell.

2.1.2 Pressurization with 120/80 mmHg

For simulation of the physiological blood pressure, the AFM setup was customized with a tight pressure chamber (Figure 2.2). The chamber consisted of a rubber seal placed tightly between the cantilever holder and the substrate (cells seeded on a coverslip). An external reservoir filled with fluid was attached to the chamber with tubing passing through the cantilever holder. Thus, diastolic pressure was simulated with hydrostatic pressure exerted by the fluid in the elevated reservoir, and systolic pressure was mimicked by additionally indenting the cell with the AFM probe.

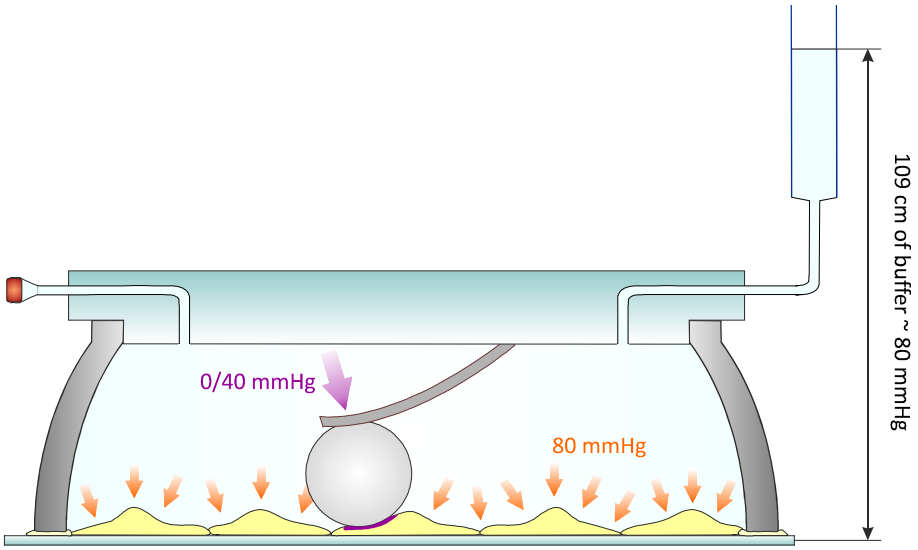

Figure 2.2. Scheme of the pressure chamber utilized for simulation of 120/80 mmHg pressure. Cells were seeded on a glass coverslip and placed under the AFM. A rubber seal was glued to the cantilever holder and pressed onto the coverslip, forming a tight fluid chamber. Two tubes connected to the chamber through the cantilever holder allowed perfusion and were used for filling the chamber with the buffer. After filling the chamber, one of the tubes was fastened, and a reservoir connected to the other one was raised to an altitude corresponding to hydrostatic pressure of 80 mmHg. An AFM cantilever with a spherical probe was repetitively indented into the cells, mimicking systolic pressure. The rubber seal was attached to the cantilever holder with glue and remained tight thanks to a layer of silicone gel sticking it to the coverslip (marked as a thin yellowish layer).

The aim of the experiment was to identify the reactions that depend on pulse pressure and are triggered locally, without engagement of the entire cell. Hence, the pressure waves exerted on the investigated cell were non-physiological in general, yet quasi-physiological over the stimulated region.

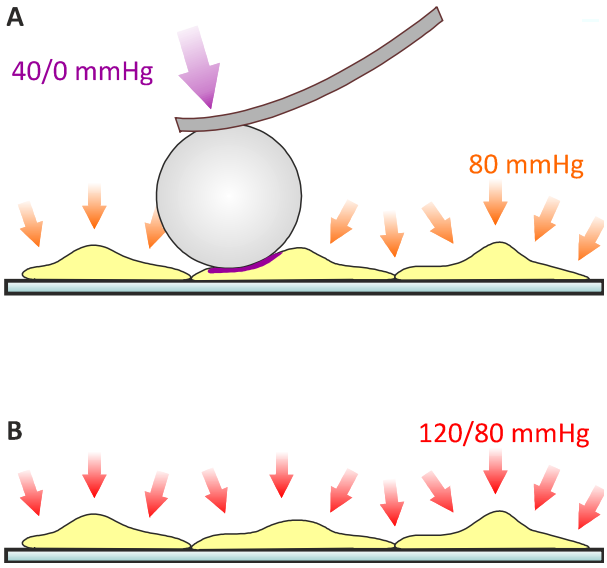

Figure 2.3. Local and global pressurization of endothelial cells. (A) The conducted experiment relies on local application of pulse pressure. Only a part of cell's surface is subjected to the pressure of 120/80 mmHg, the rest of it, as well as neighbor cells, are subjected to constant pressure of 80 mmHg. (B) In physiological conditions, the periodic pressure of 120/80 mmHg is applied over the entire surface of all cells. Nevertheless, the pressure on the surface of contact between the cell and the probe (A) is the same as the physiological pressure exerted on cells (B) – this equality allows investigation of local effects elicited by pulse pressure.

2.1.3 Shape of the pulse

The investigated cell was punched with the probe once per second, to simulate the physiological pulse rate of 60 beats per minute. Calculation of mean pressure on the area of contact over time yields the shape of the quasi-physiological pulse pressure waves.

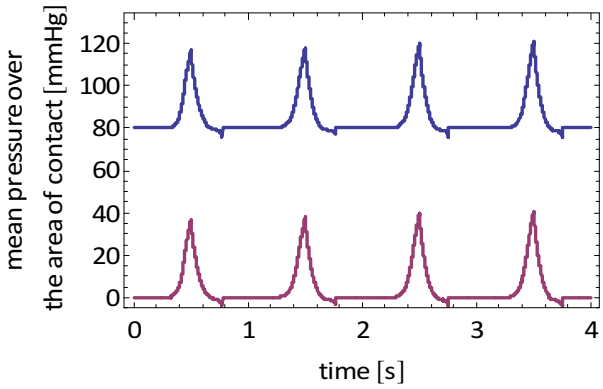

Figure 2.4. Shape of pulse pressure exerted in the experiment. The two variants are plotted: 120/80 mmHg and 40/0 mmHg. The constant hydrostatic pressure of 80 or 0 mmHg corresponds to diastolic pressure. Periodic pulse pressure waves are generated with an AFM probe and reach the value of 120 or 40 mmHg which corresponds to systolic pressure.

2.2 Control of exerted pressure

The pressure exerted on cell surface was localized and controlled taking advantage of the excellent features of the AFM: accuracy of tip positioning and precision of force measurement. The possibility of concurrent measurement of indentation into the cell and force exerted on the probe enabled quantification of pressure on the contact surface.

The area of contact between the colloidal tip and cell surface is determined using the following equation derived by Sneddon [21]:

$$\Delta z = \frac{1}{2} r \ln \frac{R + r}{R - r}, \tag{2.1}$$

where Δz is the penetration depth (indentation, see Figure 2.5), r is the radius of the circle of contact, and R is the radius of the probe. The assumptions for this model are discussed in detail in section 2.3.

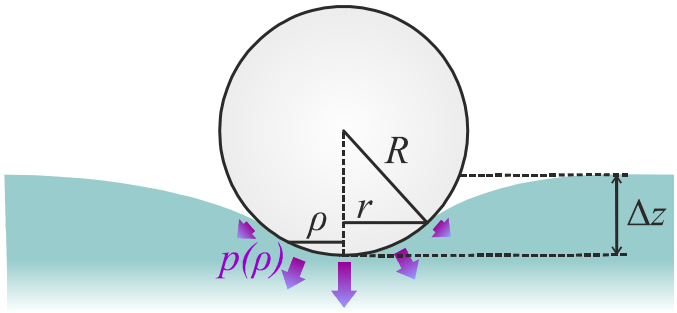

Figure 2.5. Illustration for the Sneddon theory of contact between a rigid sphere and an elastic half-space. The spherical probe indents into the sample: knowing the total load on the probe F and the penetration depth Δz, we calculate the radius r of the circle of contact, as well as the distribution of pressure $p(\rho)$ over the contact area.

The pressure exerted on the contact area by the spherical probe is not uniform. Basing on Sneddon's theory, the distribution of pressure over the surface of contact is described by the following formula [22]:

$$p(\rho) = p_0 \sqrt{1 - (\rho/r)^2}. \tag{2.2}$$

The function is parameterized with circle radius ρ (see Figure 2.5), which runs from 0 to r. p_0 is the pressure in the lowest point of contact surface:

$$p_0 = \frac{3}{2} \frac{F}{\pi r^2}, \tag{2.3}$$

where F is the total load on the probe (controlled in the experiment), and πr^2 is the area of the circle of contact. The cumulative distribution function of pressure over the area of contact $\mathrm{CDF}(p)$ is given by the formula:

$$\mathrm{CDF}\big(p(\rho)\big) = \frac{S(p < p(\rho))}{S_r}, \tag{2.4}$$

where S_r is the area of the surface of contact, *i.e.* a spherical cup with curvature radius R, and edge circle radius r. The pressure p is higher than $p(\rho)$ over a spherical cup of area S_ρ. Hence,

$$S\big(p < p(\rho)\big) = S_r - S\big(p > p(\rho)\big) = S_r - S_\rho. \tag{2.5}$$

Thus, it follows:

$$\mathrm{CDF}\big(p(\rho)\big) = 1 - \frac{S_\rho}{S_r}. \tag{2.6}$$

The area S_ρ of a spherical cup is given by an integral over spherical coordinates θ, φ (Figure 2.6):

$$S_\rho = \int_0^{2\pi} \mathrm{d}\varphi \int_{\theta_\rho}^{\pi} R^2 \sin\theta \, \mathrm{d}\theta = 2\pi R^2 \left(1 - \sqrt{1 - \rho^2/R^2}\right). \tag{2.7}$$

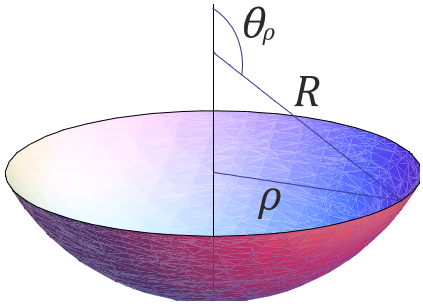

Figure 2.6. A spherical cup with curvature radius R, and edge circle radius ρ. The area of the cup is calculated by integration of the surface element $R^2 \sin\theta \, \mathrm{d}\theta \, \mathrm{d}\varphi$ over the surface boundaries: $\theta_\rho < \theta < \pi$, $0 < \varphi < 2\pi$.

Hence, the cumulative distribution function is given by:

$$\mathrm{CDF}\big(p(\rho)\big) = 1 - \frac{1 - \sqrt{1 - \rho^2/R^2}}{1 - \sqrt{1 - r^2/R^2}}. \tag{2.8}$$

We shall eliminate the parameterization with circle radius ρ. Equation (2.2 yields a substitution:

$$\rho^2 = r^2 \left(1 - \left(\frac{p(\rho)}{p_0}\right)^2\right). \tag{2.9}$$

Therefore, we get:

$$\mathrm{CDF}(p) = 1 - \frac{1 - \sqrt{1 - r^2/R^2\left(1 - \left(\frac{p}{p_0}\right)^2\right)}}{1 - \sqrt{1 - r^2/R^2}}. \tag{2.10}$$

In the regime of our experiment we have $r^2/R^2 \ll 1$ (actual values: $r \approx 5\ \mu\mathrm{m},\ R \approx 25\ \mu\mathrm{m}$), so one may approximate the formula (2.10 with its limit for $r^2/R^2 \to 0$:

$$\mathrm{CDF}(p) \xrightarrow{r^2/R^2 \to 0} \left(p/p_0\right)^2. \tag{2.11}$$

The cumulative distribution function of pressure (calculated according to equation (2.10) is presented in Figure 2.7. The parabolic shape indicated by equation (2.11) is clearly visible.

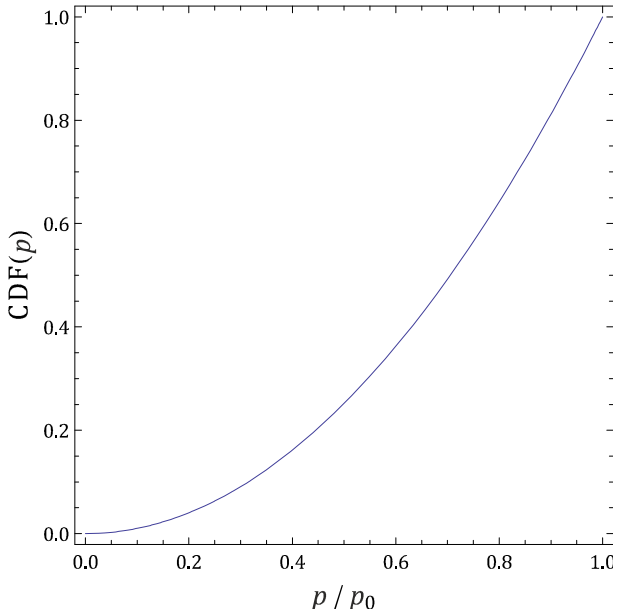

Figure 2.7. Cumulative distribution function of pressure over the area of contact, calculated according to formula (2.10), basing on Sneddon's theory. It is evident that low pressure (below $0.2\ p_0$) acts on a very small part of the contact surface. Hence, although the pressure distribution on contact surface is not uniform, one may state that the probe exerts relatively large pressure almost over the entire area of contact.

The probability density function is derived by differentiating the CDF with respect to p:

$$\mathrm{PDF}(p) = \frac{\mathrm{d}}{\mathrm{d}p}\mathrm{CDF}(p) = \frac{2p}{p_0^2}. \tag{2.12}$$

This yields the mean value of pressure over the area of contact:

$$\bar{p} = \int_0^{p_0} p\ \mathrm{PDF}(p)\ \mathrm{d}p = \frac{2}{3}p_0 = \frac{F}{\pi r^2}. \tag{2.13}$$

Figure 2.8 visualizes the distribution of pressure for a real experimental situation. Although the surface of contact is relatively flat, the pressure distribution over the surface is notably

heterogeneous, with values ranging from 0 to 60 mmHg. The mean value of pressure over the area of contact is 40 mmHg, which corresponds to the amplitude of pulse pressure *in vivo*.

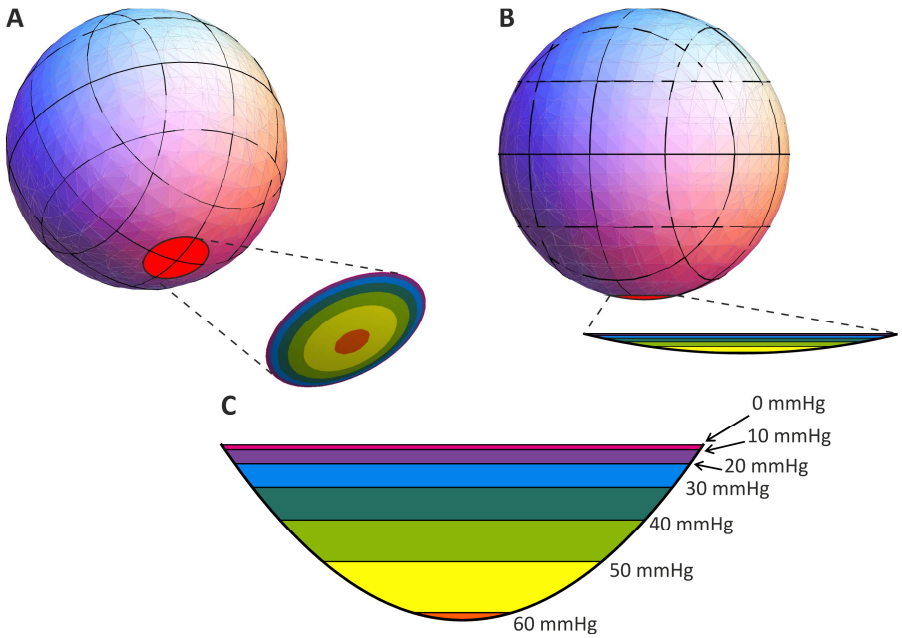

Figure 2.8. Distribution of pressure on the surface of contact between a colloidal probe and a cell. (A) A spherical probe with radius of 26 µm, indented into the cell by 1.5 µm. The circular area of contact is marked in red and has a radius of 6 µm. (B) Side view on the probe, with an enlarged cross-section of the contact area. The surface of contact is relatively flat, yet pressure varies over it dramatically. (C) Distorted cross-section of the surface of contact, with isobars painted as horizontal black lines. The rainbow-like color scale visualizes the distribution of hydrostatic pressure on the surface of contact at the moment of deepest indentation into the cell. The average pressure on the surface of contact is 40 mmHg.

2.3 Measurement of elasticity – nanoindentation spectroscopy

The elasticity of the cortical network of actin filaments is measured using nanoindentation spectroscopy. In this technique [23], an indenter is pushed into the investigated sample, normal to its surface. The deformation of the sample yields a restoring force acting on the probe. This force is measured concurrently with the displacement of the AFM cantilever relative to the substrate. Hence, one obtains a force-distance curve (Figure 2.9 A).

In an AFM setup (Figure 2.1 and Figure 2.2) the force is measured by photovoltaic detection of the cantilever's deflection, which multiplied by the spring constant of the cantilever k gives the force acting on the probe. When the probe is in contact with the sample, then any displacement of the AFM cantilever towards the sample causes further deflection of the cantilever, and further indentation into the sample. Hence, one may calculate the penetration depth into the sample by

subtraction of the cantilever's deflection from its overall displacement (Figure 2.9A). The cantilever is displaced by application of voltage to a piezoelectric crystal, whose extension (the *distance* parameter) is measured during acquisition of a force-distance curve.

Calculation of the indentation depth for every point in the contact regime of a force-distance curve yields a force-indentation curve (Figure 2.9 B). Sneddon's theory predicts a monomial dependence of the force F on the indentation Δz:

$$F(\Delta z) = \frac{4}{3}\frac{E}{1-\nu^2}\sqrt{R}\,(\Delta z)^{3/2}, \tag{2.14}$$

where E is the elasticity parameter of the cell cortex, and ν is the Poisson ratio of the sample (assumed to be 0.5, meaning perfect incompressibility). Fitting this formula to a force-indentation curve gives the numerical value of the elasticity parameter of the sample.

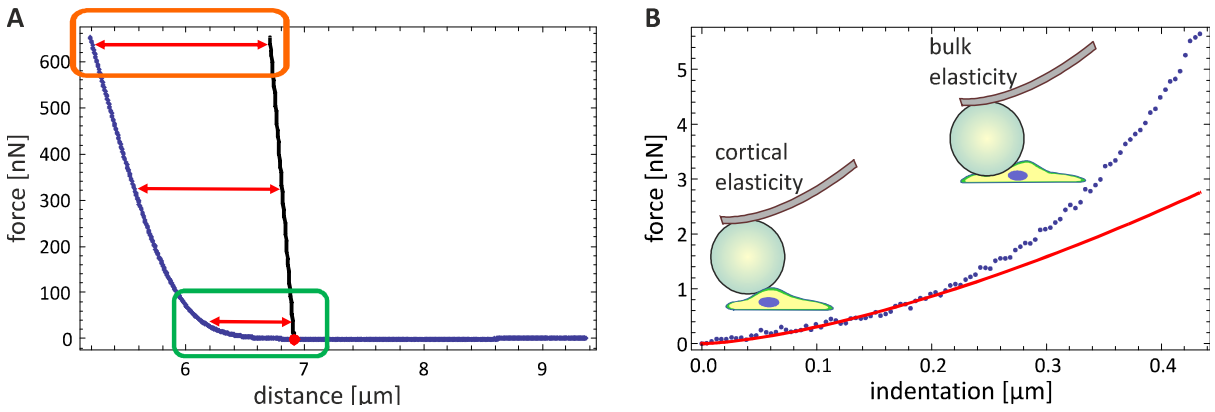

Figure 2.9. Acquisition of force-distance curves enabled concurrent control of pressure exerted on the cell's surface and measurement of the elasticity of the cell cortex. (A) The indentation depth into the sample (red lines) is calculated for every value of deflecting force. The red dot marks the contact point, and the black line depicts the force-displacement relation for an AFM cantilever. Knowing the indentation exerted by maximal force (high force regime, orange box), we derive the amplitude of pressure (formulae (2.1) and (2.13)). The relation between force and indentation in the low force regime (green box) yields the elasticity of the cell cortex. (B) Elasticity parameter of the cortical layer of filamental actin is calculated by fitting formula (2.14) to the force-indentation curve in the regime of low indentation. The regime of high indentation gives information about bulk elasticity of the cell.

The Sneddon's theory of elastic contact features certain assumptions, which do not entirely hold true in the conducted experiment. Nevertheless, the model seems to be applicable for the studied problem. The model assumes that the probe is ideally rigid – this condition is actually not fulfilled in the experiment, yet it is justified by the dominance of sample deformation over probe

deformation [24]. It is also assumed, that there are no surface forces acting between the cantilever and the probe – indeed, adhesion forces in this experiment are negligible relative to the elastic forces and the hydrodynamic drag, as revealed by comparison of force-distance curves for approach and retraction of the probe. Furthermore, the indenter is assumed to be pushed normal against a flat surface. The surface of an endothelial cell is by no means flat, however in our case the constraints of the investigated cells considerably exceeded the diameter of the area of contact, and the force was loaded on the central part of the cell, where the tilt of the surface is relatively low. Finally, it is assumed that the indented half-space is ideally elastic and uniform – this postulate is not fulfilled, as a living cell consists of components of various mechanical properties. Hence, elasticity is evaluated only for the regime of small indentations (< 150 nm), which corresponds to the submembraneous network of cytoskeletal fibers [25].

Concurrently to the measurements of the elasticity parameter of the indented region, the changes in height of that area were estimated, basing on the calculation of the contact point of the cell – a downshift of the probed surface results in a greater extension of the tip scanner at the point of contact between the surface and the probe.

2.4 Fluorescence microscopy

Concurrently to the measurement of local height and mechanical properties of the investigated cell, fluorescence measurements were performed to examine the effects of local stimulation on the structure and functioning of the entire cell. Three types of stains were used: Lifeact (stains the actin filaments), Hoechst (stains the nucleus) and DAF-FM (stains NO, creating a fluorescent form DAF-FM T). The fluorophores were not excited by the AFM laser which emitted at the wavelength of 880 nm.

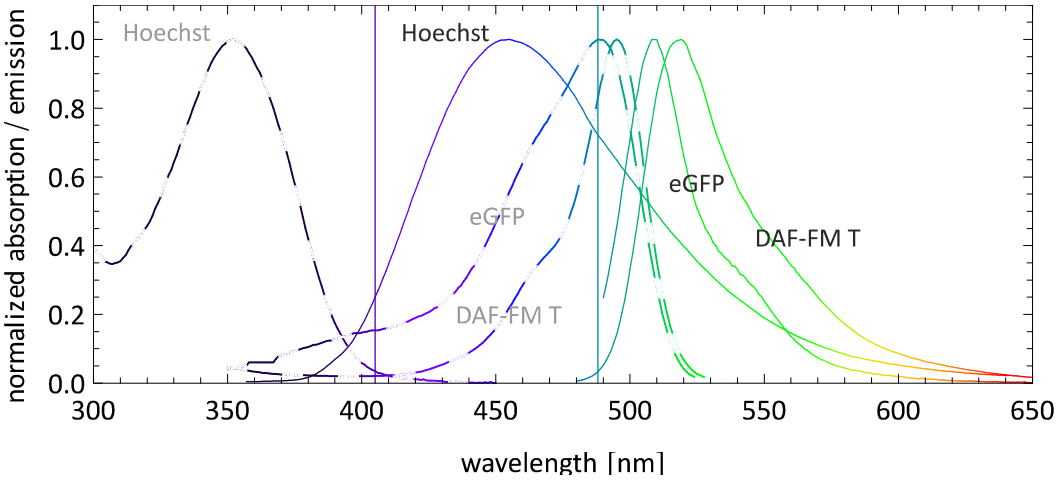

Figure 2.10. Excitation/ emission of fluorophores used in the experiment. Absorption and emission spectra are plotted with dashed and solid lines, respectively. Wavelengths of the two lasers (405 nm, 488 nm) are marked with vertical lines. The spectra of eGFP and DAF-FM T overlap substantially, hence they could not be used concurrently in the experiment – illumination with 488 nm laser light would excite both fluorophores. Hoechst may be used simultaneously with eGFP or DAF-FM thanks to the minor overlap of the absorption spectra. The laser wavelength 405 nm lies on the edge of the absorption spectrum of Hoechst, consequently a relatively high laser power has to be applied.

2.4.1 Lifeact staining of actin filaments

In order to interpret the changes in the elasticity of the cell cortex, filamental actin was stained by transfection of the cells with Lifeact eGFP. In this method cells are transfected with the Lifeact peptide ligated to the enhanced green fluorescent protein (eGFP). Lifeact is a 17- amino acid peptide which binds to F-actin and does not interfere in actin dynamics, *i.e.* its expression and polymerization in living cells [26]. The transfection relies on delivering the Lifeact-eGFP DNA plasmid via endocytosis into the cell's nucleus (Figure 2.11). This process is facilitated by a transfection reagent FuGENE6 which forms liposomes and incorporates the Lifeact-eGFP plasmid, forming a DNA-lipid complex. The vesicles enter into the cell via endocytosis. The plasmid may be released from the endosome and enter the nucleus, where it would be transcribed to an mRNA molecule. Then, the mRNA is translated in a ribosome, thus Lifeact-eGFP is expressed and released into the cytosol.

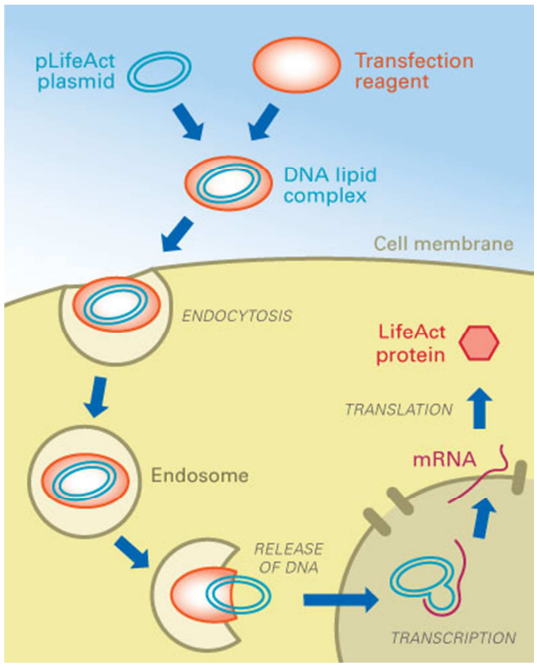

Figure 2.11. Transfection of a cell with Lifeact-eGFP. Thanks to a fancy biotechnological trick, the fluorophore is self-synthesized by the cell. A liposome of the FuGENE6 lipid forms around the Lifeact-eGFP DNA plasmid, and is delivered to the nucleus via endocytosis. Then it is transcribed to mRNA and translated in a ribosome to the Lifeact-eGFP protein. The figure is reprinted from the manufacturer's website *www.ibidi.com*.

In the reported experiment, the Lifeact-eGFP transfection was successful only for less than 5% of the cells. Nevertheless, it was always possible to find a fluorescent cell in the field of view of the fluorescence microscope. The conducted experiment deals with phenomena happening on the level of a single cell, therefore the low efficiency of the transfection did not cause difficulties in this case.

The eGFP is a 293- amino acid protein, with an excitation peak at 488 nm and an emission peak at 507 nm. With the Lifeact-eGFP protein bound to F-actin, the dynamics of filamental actin may be visualized in a living cell (Figure 2.12). In the conducted experiment, the deformation of actin cytoskeleton and disruption of stress fibers were traced during application of pulse pressure, by means of a confocal fluorescence microscope.

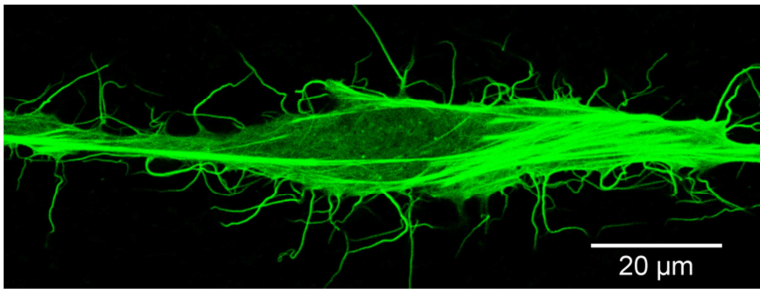

Figure 2.12. Fluorescence image of a Lifeact-eGFP transfected cell. The focal plane coincides with the surface of the coverslip, therefore the filopodia and the basal stress fibers are clearly visible. Fluorescence images of actin filaments allow observation of the deformation of stress fibers, and polymerization of cortical actin.

2.4.2 Hoechst staining of nucleus

Staining of the nucleus enabled examination of its deformation or displacement due to stimulation with the probe. Hoechst 33342 dye was used to stain the nuclei of living endothelial cells – the dye is cell-permeant and *supravital* (cells survive treatment with this compound). It binds to the minor groove of double stranded DNA [27], enabling bright blue fluorescence.

The cells were loaded with the stain by incubating them in a solution of Hoechst in the buffer for 30 minutes. After binding to dsDNA, the dye has an absorption peak at 350 nm and an emission peak at 461 nm. The unbound molecules have weak green fluorescence (510-530 nm).

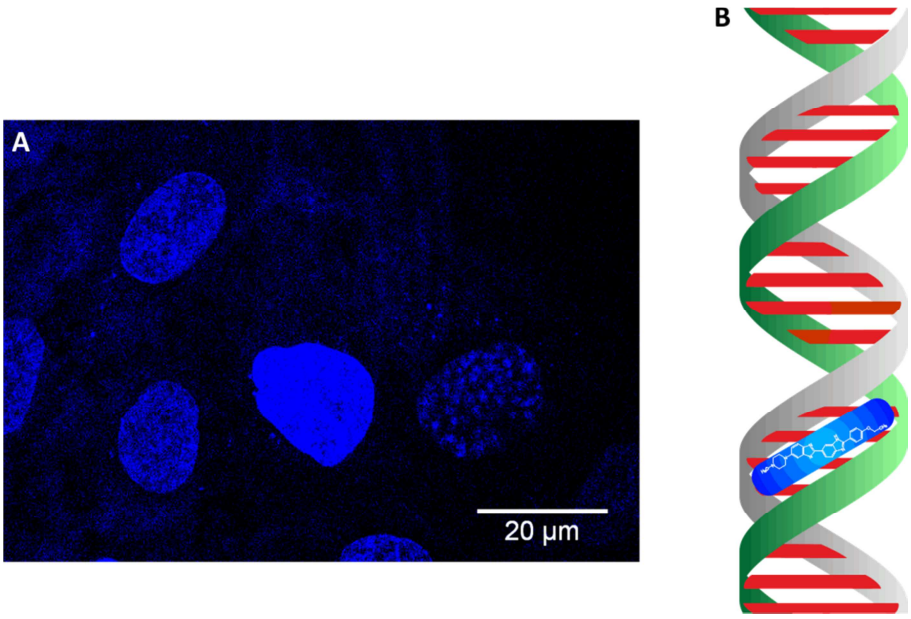

Figure 2.13. Staining of the nuclei with Hoechst 33342. (A) Fluorescence image of cell nuclei stained with Hoechst 33342. (B) Binding of the Hoechst dye to the minor groove of double stranded DNA enables bright blue fluorescence of the molecule, excited by UV light. The unbound dye has week green fluorescence (510-530 nm).

In the experiment, Hoechst was used to visualize the displacement of the nucleus of the stimulated cell during application of pulse pressure. The image of the nuclei was also used for refocusing of the CLSM objective (see section 2.5.1).

2.4.3 DAF-FM staining of nitric oxide

NO was stained using a fluorescent marker DAF-FM (diaminofluorescein-FM) [28]. The dye is delivered to the cells in the diacetate form (DAF-FM DA) which is cell-permeant and quickly transformed into the water-soluble DAF-FM by esterases in the cytosol. The dye reacts directly with NO^+ equivalents, which are auto-oxidized forms of NO. Hence, in the presence of oxygen, DAF-FM binds to NO, yielding the highly fluorescent triazolofluorescein (DAF-FM T). Thanks to presence of fluorine in the structure of the dye, the fluorescence intensity does not depend on pH over a broad range of values (pH > 6).

DAF-FM T has an absorption peak at 495 nm and a fluorescence peak at 515 nm. The triazole form (DAF-FM T) has a 160-fold greater quantum efficiency than the diamine form (DAF-FM) and is insensitive to photobleaching [28,29].

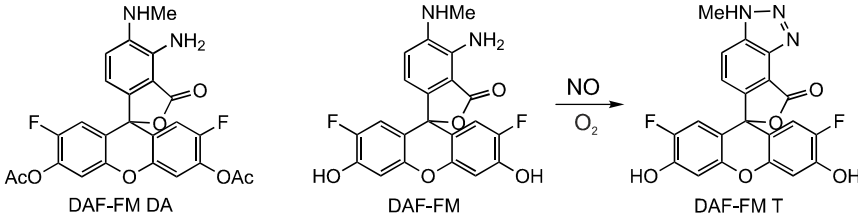

Figure 2.14. Structures of the different of forms of DAF-FM. The cell-permeant diacetate form is transformed into the DAF-FM form in the cytosol. DAF-FM reacts with auto-oxidized forms of NO, yielding the highly fluorescent DAF-FM T by nitrosation and dehydration. Figure adapted from the literature [28].

DAF-FM T is cell-impermeant, but it easily diffuses in the cytosol (Figure 2.15). Therefore, an increase in the concentration of NO in the cytosol results in a rise of total fluorescence intensity from the entire cell. Additionally, the fluorescence of DAF-FM T enables determination of the cell's shape and its deformation.

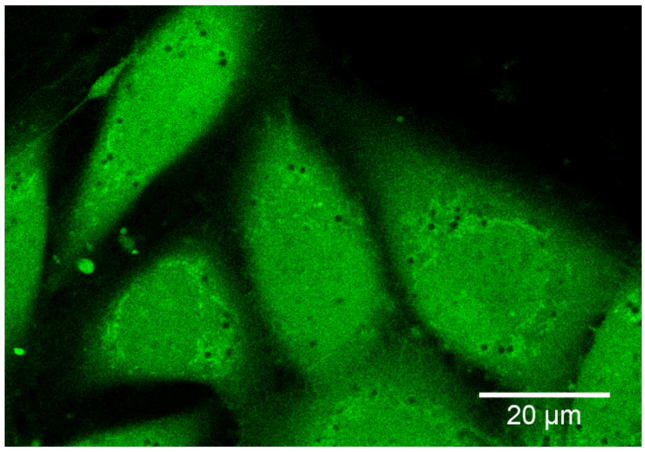

Figure 2.15. Fluorescence image of cells loaded with DAF-FM. The DAF-FM T fluorophore diffuses in the cytosol and emits fluorescence from the entire bulk of the cell, enabling determination of the cell's shape.

2.5 Artifacts and experimental difficulties

The main focus of the thesis is the design and launch of a novel AFM-based setup for local pressurization of an individual endothelial cell and concurrent measurement of its features by means of nanoindentation spectroscopy and CLSM. To achieve this goal, several technical obstacles were to be overcome. During the time assigned for the study, all emergent artifacts were eliminated, yielding meaningful and reliable results. This sections gives a description of the experimental difficulties encountered in the study.

2.5.1 Drift of the substrate

Two types of fluid chambers were used in the experiments: BioCell delivered by JPK Instruments (Figure 2.1) and the custom designed pressure chamber (Figure 2.2). In both fluid chambers we

observed a substantial vertical drift of the substrate: the cells imaged with the confocal microscope moved gradually out of focus.

The drift may be explained as an effect caused by a few factors:

- deformation of the rubber seal, resulting in a change of the force exerted on the edges of the coverslip (BioCell and pressure chamber),
- expansion/ contraction of the layer of silicone gel between the rubber seal and the coverslip, and of the glue assembling the coverslip to the metal inlay of PetriDishHeater (pressure chamber),
- force exerted by the meniscus of immersive oil on the bottom surface of the coverslip (BioCell and pressure chamber),
- bending of the coverslip due to elevated pressure in the chamber (120/80 mmHg in the pressure chamber).

The occurrence of the drift in BioCell was quite surprising, considering the fact that this fluid chamber was designed specially to assure stable conditions of biological AFM trials. The rate of the movement was on the order of 0.5÷1 μm/h, hence the artifact should become evident only in trials lasting a few hours.

In the case of the pressure chamber, the drift could lead to far greater displacements, reaching 8 μm in the extreme case shown in Figure 2.17. Such dramatic drift was caused mainly by the contraction of the layer of silicone gel between the rubber seal and the coverslip (Figure 2.2), used for tightening of the chamber. Whenever the position of the AFM head was readjusted with the motors, a slow movement of the sample followed, due to the elasticity of the gel. It is remarkable that rubber seals are frequently used in AFM setups to tighten the fluid cell. Yet one does not expect the liquid chamber to be tight, hence the silicone gel is usually unnecessary.

The drift of the substrate resulted in biased measurement of contact point height (Figure 2.16). The apparent shift of the contact point may result both from the change in height of the indented region, and from the movement of the coverslip.

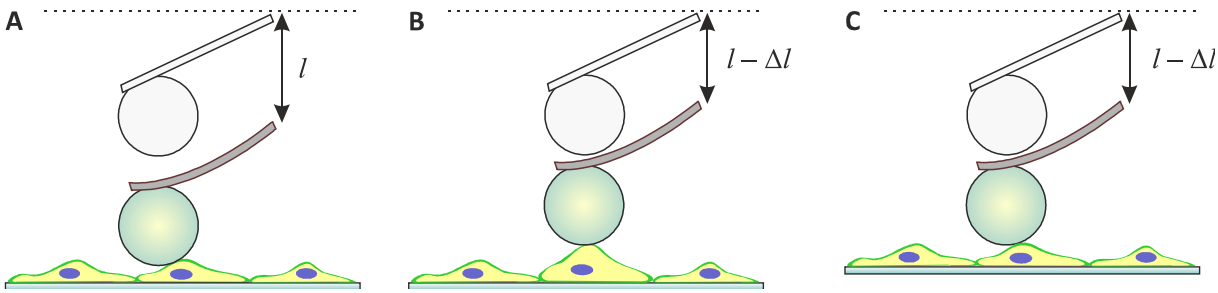

Figure 2.16. Drift of the substrate falsified the measurement of contact point height. The scanner extension required to reach contact between the sample and the probe changed from l (in A) to $l - \Delta l$ (in B and C). This shift could be caused by an increase in cell height (B) or by an upward displacement of the coverslip (C).

The drift of the substrate was controlled and compensated by readjusting the focus of the CLSM before acquisition of every image. The microscope was focused on the nuclei of cells in the neighborhood of the stimulated cell – we believe that those nuclei were not dramatically deformed or displaced (in Z direction) during the experiment. It was challenging to determine the exact position of the focal plane using the live acquisition mode of CLSM, in the short period of time between subsequent series of pulse pressure waves. Therefore, in each intermission, the live mode was used for coarse focusing, and then a Z-stack was acquired, consisting of 4 slices, with the center at the coarse focus and a step size of 0.3 µm. After the experiment, all Z-stacks were examined, and the frame in focus was chosen for quantitative analysis.

The procedure of compensation of the substrate drift is illustrated in Figure 2.17. The drift of the focal plane (B) was subtracted from the trace of contact point height (A), yielding the true movement of the contact point in time (C).

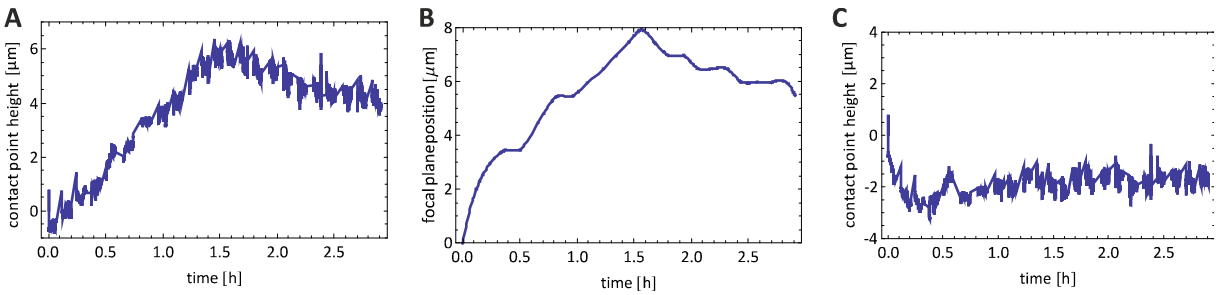

Figure 2.17. Compensation of the substrate drift. The raw record of contact point height (A) is tremendously biased by the drift of the sample. The AFM head was retracted by a few micrometers right before the beginning of the experiment, resulting in slow (~ 1.5 h) contraction of the layer of silicone gel between the rubber seal and the coverslip. This contraction appears in graph (A) as a gradual increase in contact point height. The measurement was interrupted every 5 minutes for acquisition of a confocal Z-stack of fluorescence images. Post-processing of the images enabled determination of the movement of the focal plane (B). The change in the position of the focal plane (B) was subtracted from the raw record of contact point height (A), yielding the true displacement of the contact point (C). The saw-like pattern in (C) results from recovery of the cell surface during the intermission between subsequent series of pulse pressure waves.

2.5.2 AFM laser interference

Pulse pressure was applied to endothelial cells via a spherical indenter made of polystyrene. The probe was transparent to the light of the AFM laser (wavelength 880 nm). For large probes, refraction of the laser beam on the surface of the probe, together with the reflection on the surfaces of the coverslip and the probe, resulted in interference of the rays constituting the laser beam. The observed phenomenon is known in the literature as Newton rings. In this effect, the incident light is scattered by the system into all directions within the plane of incidence. In other words, the energy of the beam is spatially redistributed, so that the intensity of the light leaving the system oscillates with respect to the inclination angle. Change in the distance between the probe and the glass surface results in a shift of the angular interference pattern. Hence, during acquisition of a force-distance curve, one should expect oscillations of the intensity of the light incident on the upper and downer quadrants of the AFM photodiode. These oscillations are manifested as periodic changes of the vertical deflection signal (Figure 2.18), which is calculated by subtraction of the voltages generated on upper and downer quadrants of the photodiode.

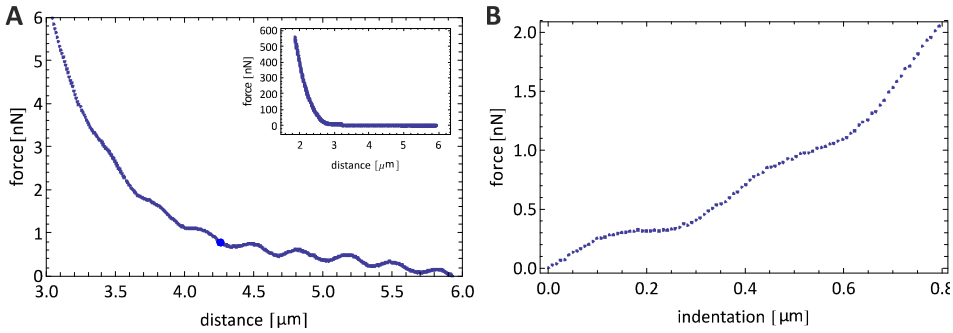

Figure 2.18. Oscillations on a force-distance curve, resulting from interference of the AFM laser beam on the probe-glass system. (A) When the spherical probe approaches the reflexive surface of the glass coverslip, the emergent pattern of Newton rings changes with varying distance between the probe and the glass surface. Thus, the vertical deflection signal oscillates during acquisition of the force-distance curve. The period of the oscillations is 440 nm, which corresponds to half of the wavelength of the AFM laser. The estimated position of the contact point is marked with a blue dot. (B) Force-indentation curve, calculated for the force-distance curve presented in (A), assuming the marked position of the contact point. The oscillations of the vertical deflection signal precluded calculation of the elasticity parameter, as the slope attributable to the cell cortex was dominated by the artifact.

The presented explanation of the observed artifact is supported by the fact that the period of the oscillations on the force-distance curve is equal to half of the wavelength of the AFM laser beam (440 nm = 880 nm / 2). Furthermore, the effect is emergent only when the probe is less than ca. 50 μm ($\approx 2R$) above the surface of the coverslip – hence, the interference takes place in the probe-glass system, not in the probe-cantilever system. Additionally, the artifact was noted only when large spheres (R > 15 μm) were used. The latter observation eliminates the possibility of interference between the surfaces of the cantilever and the coverslip. The amplitude of the oscillations was always greater for curves acquired in air than in liquid – this finding may be explained by the larger difference in refractive indices between polystyrene/ glass and air ($\sim$ 1.57/1.52 vs. 1.00), than between polystyrene/ glass and water ($\sim$ 1.57/1.52 vs. vs. 1.33).

Filtering of the oscillations at the level of post-processing was very difficult and ineffective, for two principal reasons. Firstly, the analytical formula for the trend line (real force-distance curve) was not known. Secondly, the amplitude of the oscillations varied on a single curve, and those variations could not be described by any simple model. Decomposition of time series failed both for additive and multiplicative model. Therefore, hardware solutions were preferred to avoid the artifact.

Initially, we tried gluing color dyed polystyrene microspheres (Phosphorex) to cantilevers, expecting extinction of the laser interference. Surprisingly, the artifact sustained. The spheres might not have

been totally opaque to the 880 nm light – the manufacturer was not able to provide the absorption spectrum of the dye used for coloring of the microspheres.

Finally, we decided to align the AFM laser beam not exactly at the end of the cantilever, but ca. 30 µm away from it, towards the chip (the total length of the cantilever was 110 µm). Thus, the fraction of light passing through the probe was reduced substantially, so that no interference was observed anymore. Nevertheless, calibration of the deflection sensitivity and the spring constant of the cantilever were subjected to an error of unknown magnitude, yielding a considerable variation in measured values of spring constant (see section 2.7.1).

In order to avoid the artifact, one should use spheres opaque to the AFM laser light, and/ or attach them to coated AFM cantilevers.

2.5.3 Excitation of the cantilever by the scanning laser beam

Acquisition of fluorescence images with the CLSM while indenting the cell with the AFM probe resulted in an artifact, manifested as oscillations on the force-distance curves (Figure 2.19). The cantilever was thermally excited by the scanning laser beam when the probe was in contact with the sample. Oscillations emerging during scanner extension resulted in hindered analysis of the extension curve (exactly like in previous section).

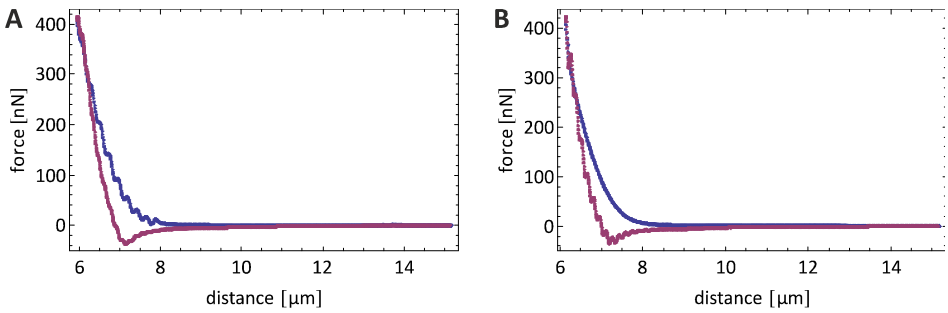

Figure 2.19. Excitation of the cantilever by the laser beam. When force-distance curves were acquired while scanning with the CLSM, the AFM cantilever was thermally excited by the incident laser beam. The cantilever was locally heated by the focused beam delivering a power of up to 2.5 mW. The local increase in temperature caused bending of the cantilever, and consequently, initiated its oscillations. This artifact was recorded both on the extension part (A) and the retraction part (B) of force-distance curves. Any oscillations on the extension curve precluded calculation of the elasticity parameter (see section 2.5.2), whereas an artifact on the retraction curve did not hamper data analysis.

The artifact was occasional, it appeared once per ca. 30 curves. Hence, one may conclude that acquisition of fluorescence images did not obstruct the AFM experiment – the corrupted curves could be removed from the data set. However, the reverse statement was not true – application of

pulse pressure did impede concurrent fluorescent imaging of the stimulated cell, due to autofluorescence of the AFM probe.

2.5.4 Autofluorescence of the AFM probe

The conducted experiment consisted of concurrent monitoring of different features of the pressurized cell, using AFM and CLSM. In order to visualize changes in the structure of the cell, one should acquire its images without the indenter pushed into the bulk. This could be achieved within the period when the probe was out of contact with the sample. Such moments constituted ca. 70% of the experiment: the ramp size of the acquired curves was 10 µm, and only a section of ~ 3 µm pertained to the contact regime. Nevertheless, the period of ca. 0.7 second between acquisition of two subsequent curves was not enough to record a fluorescence image of satisfactory quality (at least 2 seconds were required). Hence, the images acquired during application of pulse pressure contained an artifact: a snapshot of the probe indenting into the cell (Figure 2.20).

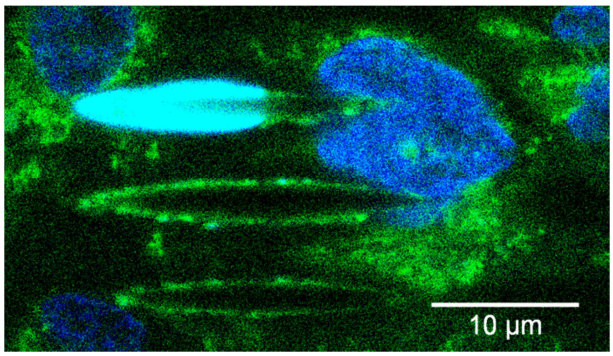

Figure 2.20. Autofluorescence of the AFM probe recorded on a confocal laser scan, acquired concurrently with application of pulse pressure. The elliptical features originate from scanning over the indenting autofluorescent probe with the laser beam. The beam scans horizontally (fast scan), moving downwards (slow scan). The upper and downer parts of the ellipse correspond to extension and retraction of the scanner. Force-distance curves were acquired once per second. The acquisition of the image lasted 2.67 seconds, therefore there are 3 elliptical traces of the probe in the image.

Potentially, one could stop the acquisition of the frame for the 0.3 second period of contact between the probe and the cell, and continue once the probe was out of contact again. Alas, this solution was not feasible due to low adaptability of the CLSM setup, and lack of protocols for communication between the AFM and the CLSM. Consequently, AFM and CLSM were applied alternately: the cell was pressurized and monitored with the AFM for 5-10 minutes, and then imaged with the CLSM for 0.25-2.5 minutes. This sequence was executed repetitively for a period of ca. 2.5 hours.

2.6 Processing of force-distance curves

Force-distance curves were analyzed with JRobust software created by Paweł Hermanowicz [30]. This software has an implemented algorithm to estimate the position of the contact point on a force-distance curve [31,32]. Once the contact point is found, the force-indentation curve is calculated, and formula (2.14) is fitted to that curve, yielding the value of the elasticity parameter E. The software has a solution to choose the appropriate range of penetration depth, which corresponds to the cell cortex (Figure 2.21). The elasticity parameter is calculated pointwise [33], *i.e.* with indentation running from $\Delta z = 0$ to the maximal possible penetration depth. As long as the indentation depth is in the region of the cell cortex, the pointwise elasticity parameter approaches the real elasticity parameter of the cortex. When the depth exceeds the thickness of the cortex, the pointwise elasticity parameter deviates from the cortical E towards bulk elasticity parameter.

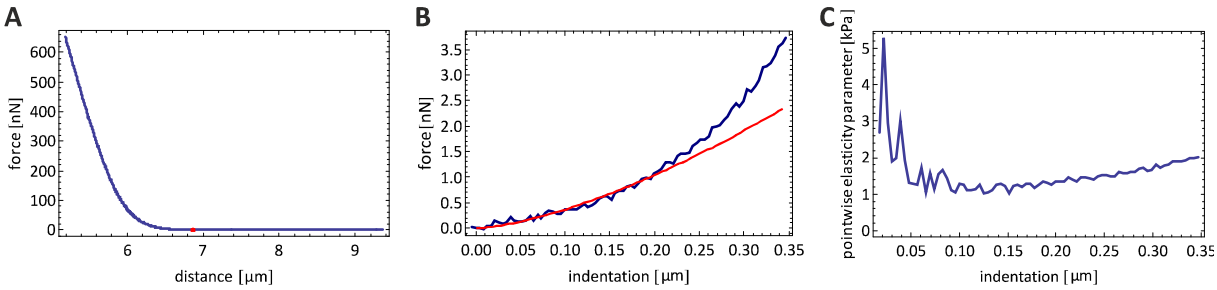

Figure 2.21. Estimation of the elasticity parameter in JRobust software. (A) A force-distance curve, with the estimated position of the contact point marked in red, which is calculated automatically by the software. (B) The force-indentation curve (blue), calculated basing on the position of the contact point. For the sake of legibility, only a small part of the curve is shown, concerning only the regime of low indentation. The red line is the fit of the Sneddon's formula (2.14) to the regime of indentation corresponding to the cell cortex. (C) Pointwise elasticity parameter E plotted against indentation Δz. Up to an indentation of ca. 0.15 µm the elasticity parameter approaches a limit value. At deeper penetration, the pointwise elasticity parameter rises towards the value of bulk elasticity parameter. Therefore, the software assumes the value $\sim$ 0.15 µm as the thickness of the cortex, and fits the Sneddon's formula to this range of indentation.

The software analyzes each curve independently, not taking into account that they constitute a time series. Consequently, the elasticity parameter and contact point position have a very high level of noise when plotted against time. Hence, the graphs showing the temporal changes of elasticity and height of the indented region (section 3.1) are smoothed over time.

2.7 Experimental

2.7.1 Atomic force microscopy

AFM measurements were performed using a Nanowizard III microscope (JPK Instruments). Two fluid cells were used: BioCell (for the trials with 40/0 mmHg pressure) and SmallCell (for the trials with 120/80 mmHg pressure).

In the 120/80 mmHg trials, the rubber seal (part of the JPK setup) was glued to the SmallCell cantilever holder using a two-component glue (delivered with the BioCell) and lubricated on the bottom edge with silicone gel. The coverslip with cells was stuck to a metal inlay in the PetriDishHeater accessory using nail polish (manufacturer unknown). In order to reduce the bending of the coverslip due to non-equilibrated pressure, it was covered with a layer nail polish on the bottom side, omitting the central part, where the immersion oil should touch the surface.

Uncoated tipless cantilevers were delivered by MikroMasch (CSC12 series). The results reported in sections 3.1-1.1 were obtained using a polystyrene spherical probe of radius R = 22.0 μm (delivered by PolySciences, Inc.) glued to the C lever of a CSC12 chip. The nominal spring constant of the cantilever was 0.6 N/m. After gluing the sphere, the spring constant increased up to ca. 1 N/m – this is the mean value, however the exact value depended on the amount of material adsorbed to the probe in a given trial, and lied in the range 0.74÷1.36 N/m, measured using thermal tune method [34]. The results reported in section 1.1 were obtained using several different probes and cantilevers, with radius between 20.5 μm and 26 μm, and spring constant between 0.11 N/m and 3.24 N/m. The probes were attached to the cantilever according to a technical note published by JPK Instruments [35]. The glue was UHU Endfest 300.

Force-distance curves were acquired once per second, and the ramp size of a curve was 10 μm, hence the velocity of the cantilever was 20 μm/s. For probes of such large diameter the high velocity results in a considerable hydrodynamic drag – the appropriate cantilever velocity is on the order of 1 μm/s. The high velocity caused a shift of elasticity parameter towards higher values (Figure 2.22) [36]. Nevertheless, the experiment focused on temporal changes of the elasticity parameter for an individual cell – despite the shift of E, its relative changes were reliably measured.

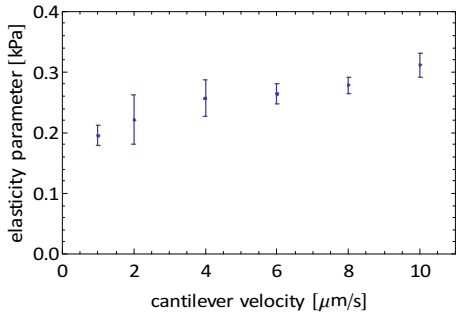

Figure 2.22. The shift of apparent elasticity parameter due to high cantilever velocity. The values of E measured at low velocity of the cantilever were merely influenced by the hydrodynamic drag exerted on the huge probe. The applied speed of 20 µm/s resulted in biased values of the elasticity parameter, however monitoring of relative changes in elasticity of an individual cell remained reliable.

2.7.2 Conditions of measurements

All experiments were performed in HEPES buffer (protocol in section 5.2), to maintain the pH = 7.4. Temperature was held at 37 ^{o}C, thanks to the Peltier heating of the BioCell, or to resistive heating of the PetriDishHeater. Monitoring of the temperature was conducted with use of the built-in thermometer of the BioCell. In the case of PetriDishHeater the setpoint value of the temperature of the heater was set to 41 ^{o}C. Then the temperature of the sample was maintained at 37 ^{o}C, as checked with a thermocouple prior to the experiments. In the case of measurements conducted in BioCell, 0.5÷1.0 ml of the buffer was exchanged every 30 minutes, in order to avoid changes in concentration of solutes in the buffer.

2.7.3 Cell culture

Bovine aortic endothelial cells (line GM7373, delivered by DMSZ [37]) were cultured in T25 culture flasks, incubated at 37 ^{o}C, 5% of CO_2, and humidity of 100%. Cells from passages 5-19 were used for the trials. Minimal essential medium (Invitrogen) supplemented with 20% fetal calf serum (PAA Clone), 1% non-essential amino acids (Invitrogen), 1% MEM vitamins (Invitrogen), and antibiotics: penicillin G (100 µg/ml, Invitrogen) and streptomycin (100 µg/ml, Invitrogen).

24 mm coverslips were coated with a collagen matrix in the central part (protocol 5.1). On the following day, endothelial cells were seeded on the coverslips (protocol 1.1) and left to grow in 35 mm dishes. After reaching confluence (1-3 days, depending on the number of seeded cells), cells were used for experiments.

2.7.4 Fluorescence microscopy

Fluorescence images were acquired using a Leica TCS SP8 confocal laser scanning microscope, equipped with an HC PL APO CS2 oil immersion objective (63x magnification, NA = 1.40).

The eGFP fluorophore was excited with a wavelength of 488 nm of an argon laser, and its emission was detected in the range 495-600 nm. The same settings were used for the DAF-FM dye. The Hoechst dye was excited with a wavelength of 405 nm of a semiconductor laser diode, and its emission was detected in the range 407-486 nm.

For all dyes, the laser power was always minimized to prevent the fluorophores from photobleaching. However, the 405 nm wavelength lies on the edge of the excitation spectrum of the Hoechst stain, hence the laser power was relatively high (0.5÷2.5 mW) compared to the laser power used for green fluorescence (0.025÷0.075 mW) – the 488 nm wavelength matches exactly the peak of eGFP excitation spectrum.

Due to an overlap of the emission spectra of Hoechst 33342 and eGFP/ DAF-FM T, sequential scanning was used: every line was scanned twice – first with the 405 nm beam, then with the 488 nm beam. Thus, no concurrent fluorescence from two fluorophores was recorded. In other words, we avoided the bleed-through artifact.

2.7.5 Cell staining

Cells were transfected with Lifeact-eGFP (kind gift from Roland Wedlich-Söldner, MPI Martinsried, Germany) 2-3 days before the trials. The procedure consists of trypsinization of the cells, diluting them in a solution of the DNA-lipid complex, and seeding them on the coverslips. The details are described in protocol 5.5.

The other dyes – Hoechst 33342 (Invitrogen) and DAF-FM DA (Merck) – were delivered to the cells right before the trials, with incubation lasting only ca. 30 minutes. The details are given in protocols 5.6 and 5.7, respectively.

3 RESULTS

In general, 26 trials were conducted, each consisting of application of pulse pressure on an individual endothelial cell for a period of several hours. The first 16 trials were performed without access to the confocal microscope, thus lacking the control over the substrate drift. Out of the 10 trials performed with the combined AFM+CLSM setup, 6 were done in BioCell (the more stable fluid cell), under atmospheric pressure, and 2 trials were performed under elevated pressure (80 mmHg). The 2 remaining experiments utilizing the CLSM are not reported, due to technical flaws occurred during those trials.

Out of the 6 experiments performed with the BioCell, in 4 trials we observed a uniform response of the cell to pulse pressure – the results of those 4 trials are presented in sections 1.1 and 1.1. The two other trials yielded different results, probably due to the application of pulse pressure on a different location over the cell surface – those results are described in section 1.1.

A few experiments were performed under hydrostatic pressure elevated up to 80 mmHg. Out of those trials, two were done with the combined AFM+CLSM setup – the results are summarized in section 1.1. The early experiments, conducted without the access to the confocal microscope, and thus without taking the substrate drift into account, were a valuable indication for the later trials: the trends observed in those preliminary experiments were verified at the later stage. Hence, their outcomes are briefly reported in section 1.1.

3.1 Height and elasticity of the pressurized region

The typical response of the cell to pulse pressure in terms of height and elasticity of the pressurized region is summarized in Figure 3.1. One may recognize the general trends: the elasticity parameter of the probed area decreases over time, and concurrently the contact point rises systematically during extended application of pulse pressure. The contact point falls substantially at the beginning of most records (Figure 3.1 A, B, C, compare with Figure 3.13) – this is interpreted as the short term response of the cell to pulse pressurization. The short term response is manifested also on some elasticity traces (Figure 3.1 A, B, compare with Figure 3.13).

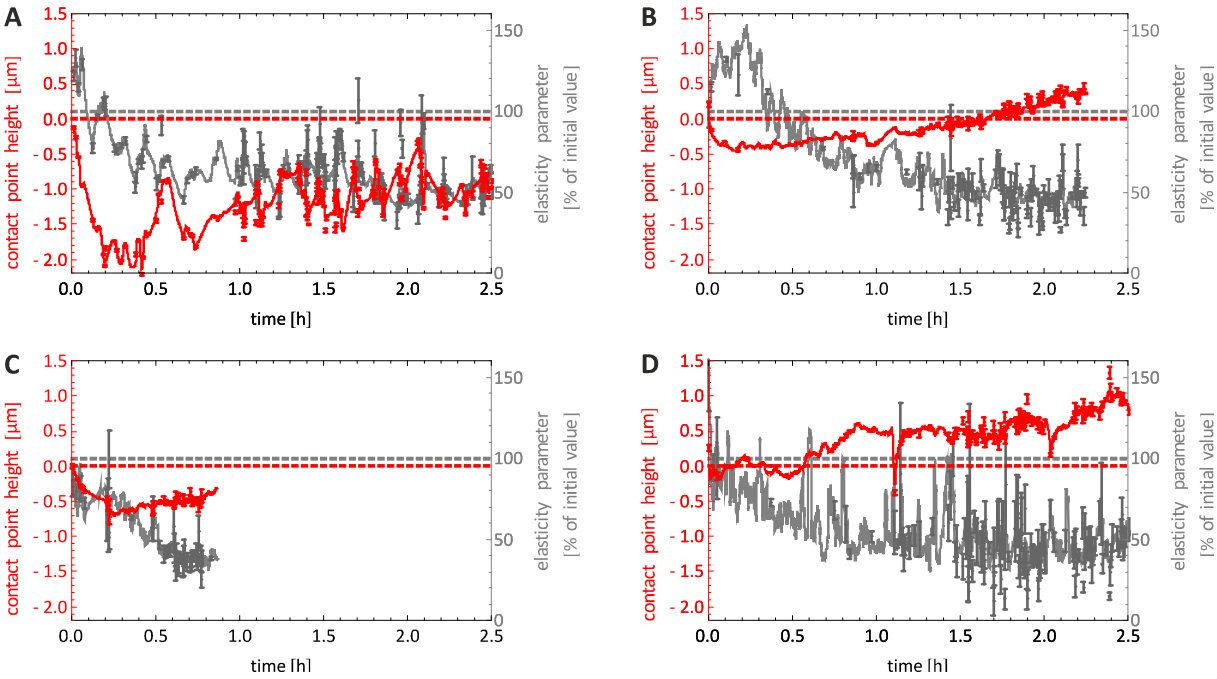

Figure 3.1. Changes in contact point height and elasticity parameter during pressurization of an endothelial cell with 40/0 mmHg pulse pressure. The graphs show the representative response of the cell, recorded in 4 different trials. Contact point height and elasticity parameter are plotted in red and grey, respectively. The initial values of the two quantities are marked with dashed lines. After an initial downfall (A, B, C), the pressurized region rose with a speed on the order of 0.5 µm/h. Concurrently, a systematic decrease in elasticity parameter was observed, down to 50% of the initial value. In some trials (A, B), the values of E measured within the first 20 minutes exceeded its initial level – this may be attributed to the resistance of the cytoskeleton to the substantial movement of the nucleus by the probe (see section 1.1).

3.2 Displacement of the nucleus

Endothelial cells were usually pressurized next to the nucleus, not right over it (for comparison, see section 1.1). Consequently, the nucleus was displaced by the indenter, which penetrated into the cell up to a substantial depth (~ 2 µm). This effect is illustrated in Figure 3.2, as an overlay of the images of the nuclei before and after stimulation with pulse pressure.

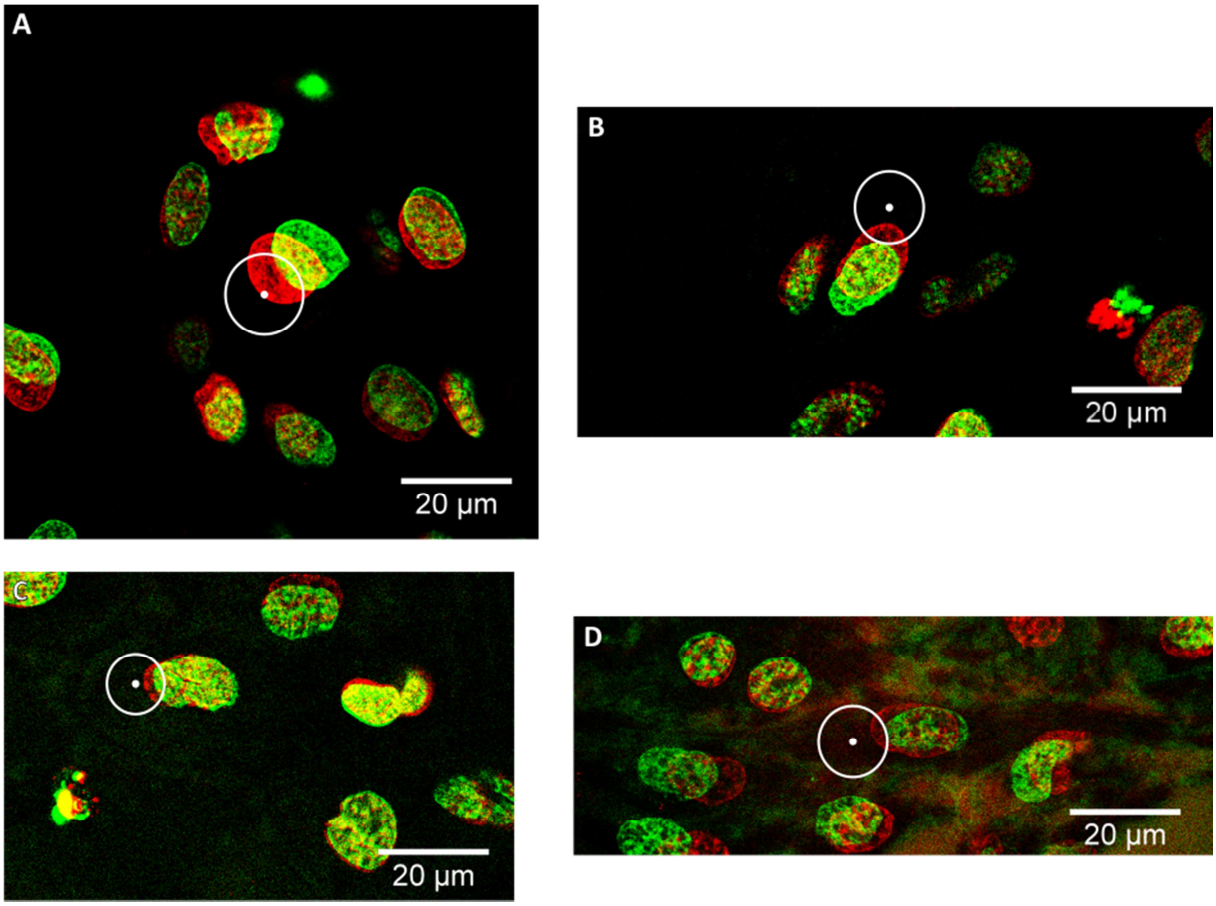

Figure 3.2. Displacement of the nucleus due to pressurization with the AFM probe. The initial and final positions of the nuclei are marked in red and green, respectively, and overlaid. The area of contact between the cell and the probe at maximal indentation is marked with a white circle. The nucleus of the stimulated cell moved away from the indenter. The more substantial displacements (A, B) coincided with the transient increase in elasticity parameter of the pressurized region (compare with Figure 3.1 A, B). Nuclei of the neighbor cells were also displaced, yet no preferable direction of that movement was noted.

The more substantial displacements of the nuclei (Figure 3.2 A, B) coincided with the transient increase of elasticity parameter over the initial value (Figure 3.1 A, B). According to the literature [38,39], the force exerted by the probe is transduced to the nucleus via the cytoskeleton, and particularly by the intermediate filaments. Therefore, we interpret the apparent stiffening of the cytoskeletal cortex as the resistance of the filamental network to the force displacing the nucleus.

3.3 Deformation of actin cytoskeletal fibers

Few experiments involved staining of the actin filaments with Lifeact. Nevertheless, we shall infer the nature of the cell's deformation from those trials. Figure 3.3 presents the general deformation of the filamental network resulting from local application of pulse pressure. One may recognize the disruption of the shell of stress fibers under the pressurized region. This phenomenon involves both the dorsal stress fibers and the perinuclear actin cap, and is better visualized in Figure 3.4 and Figure 3.5. Stretching of the stress fibers by the indenter was captured during acquisition of a force-distance curve, and is shown in detail in Figure 3.6. The records of contact point height and elasticity parameter corresponding to the trial reported in this section are presented in Figure 3.1 D.

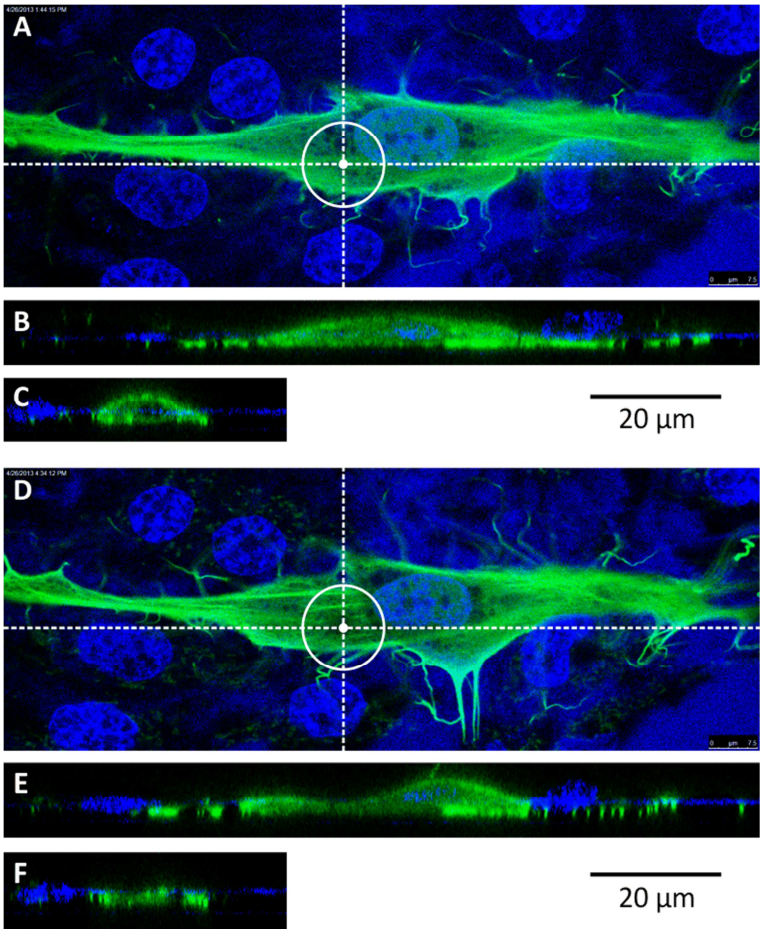

Figure 3.3. Deformation of the actin cytoskeleton due to local application of pulse pressure on an endothelial cell. The arrangement of actin filaments before and after 2.5 hours of pulse pressurization is shown in figures (A) and (D), respectively. Actin filaments were stained with eGFP (green fluorescence), cell nuclei were stained with Hoechst (blue fluorescence). The area of contact between the cell and the probe at maximal indentation is marked with a white circle. The white dashed lines mark the positions of the XZ and YZ cross-sections, shown in images B & E and C & D, respectively. The cross-sections visualize the dramatic deformation of the actin cytoskeleton induced by repetitive indenting into the cell. The shell of stress fibers embracing the cell (shown in images B and C as bright green fluorescence all over the cell's dorsal and apical surface) is disrupted by pulse pressurization (see the uniform faint fluorescence under the stimulated region in image E).

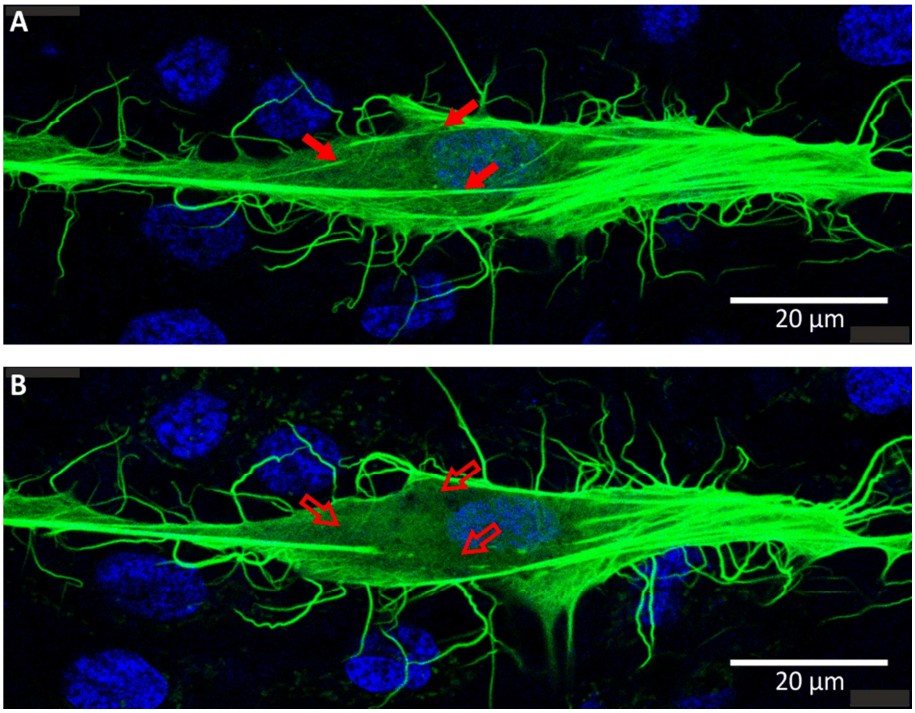

Figure 3.4. Disruption of dorsal stress fibers due to local pulse pressurization. Figures (A) and (B) visualize the arrangement of the dorsal layer of actin cytoskeleton before and after stimulation with pulse pressure. The fluorescence images were acquired along the focal plane coinciding with the surface of the substrate – thus, one may discern the dorsal stress fibers and the filopodia. The red arrows in (A) are pointing at the intact stress fibers which were disrupted later on, as indicated by the empty arrows in (B). The thickness of the imaged layer was less than 0.3 µm.

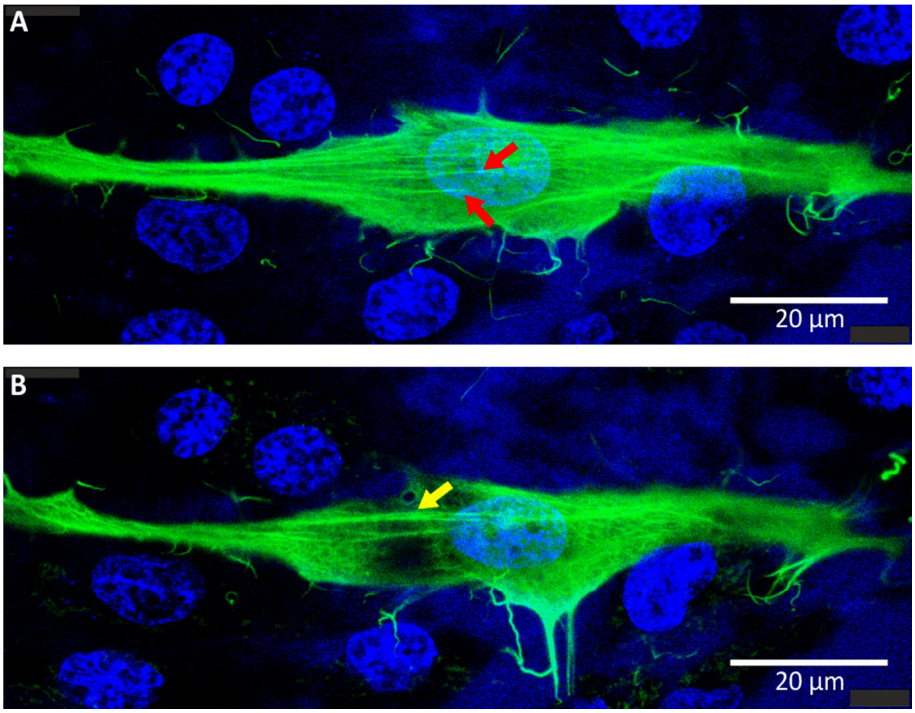

Figure 3.5. Deformation of the perinuclear actin cap resulting from application of pulse pressure. The stress fibers constituting the cap (indicated by the red arrows in image A – before pressurization) were disrupted or pushed to the side of the probe, forming thick bundles of filaments (yellow arrow in B – after pressurization). The thickness of the imaged layers in images A and B was 2.97 µm and 2.07 µm, respectively – the pictures are overlays of several subsequent XY-scans within one confocal Z-stack, covering the regime containing the perinuclear actin cap.

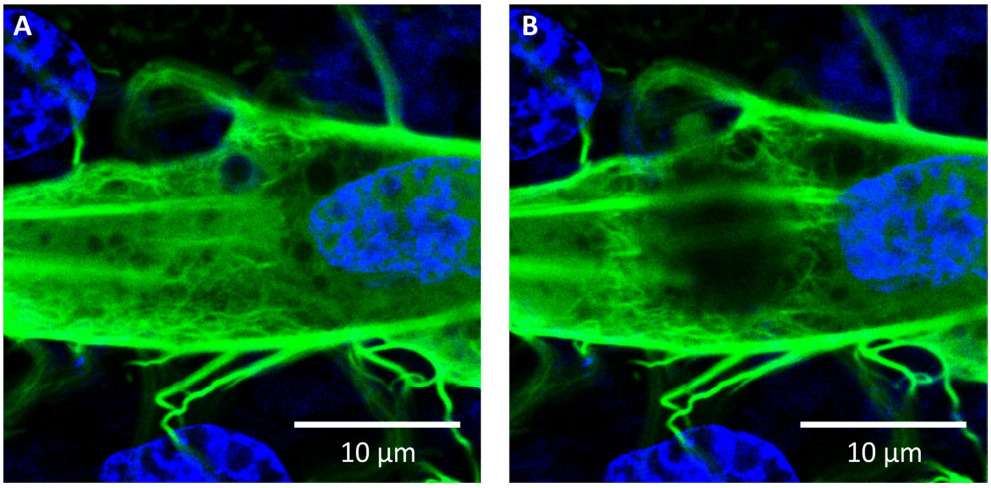

Figure 3.6. Stretching of the stress fibers and displacement of the nucleus during acquisition of a single force-distance curve. (A) Probe up and (B) probe down. The circular black region in image B is the cross-section of the probe which is indented into the cell by ~ 2 µm. The stress fibers in (B) are clearly pushed to the side of the indenter. The nucleus is also displaced by the probe (see section 1.1).

3.4 Deformation of the bulk

The dramatic deformation of the actin cytoskeleton described in the previous section seemingly contradicts the apparent rise of the contact point reported in section 3.1. However, the deformation of the cytoskeleton does not imply a change in the general shape of the cell. The contact point height describes the position of the cell membrane, and not of the cytoskeleton.

In this section, we present results showing the change in shape of the bulk of the stimulated cell. Fluorescence images of cells stained with DAF-FM are shown in Figure 3.7 and Figure 3.8. The fluorophore DAF-FM T diffused within the entire volume of the cytosol, enabling determination of the boundary between the bulk of the cell and the buffer. By comparing the three dimensional images of the cells before and after application of pulse pressure, one may assess the deformation of the bulk due to the stimulation. In this section, two examples are given: Figure 3.7 presents the deformation of the bulk of a cell pressed next to the nucleus, whereas Figure 3.8 shows the effect of pressurizing the region right over the nucleus.

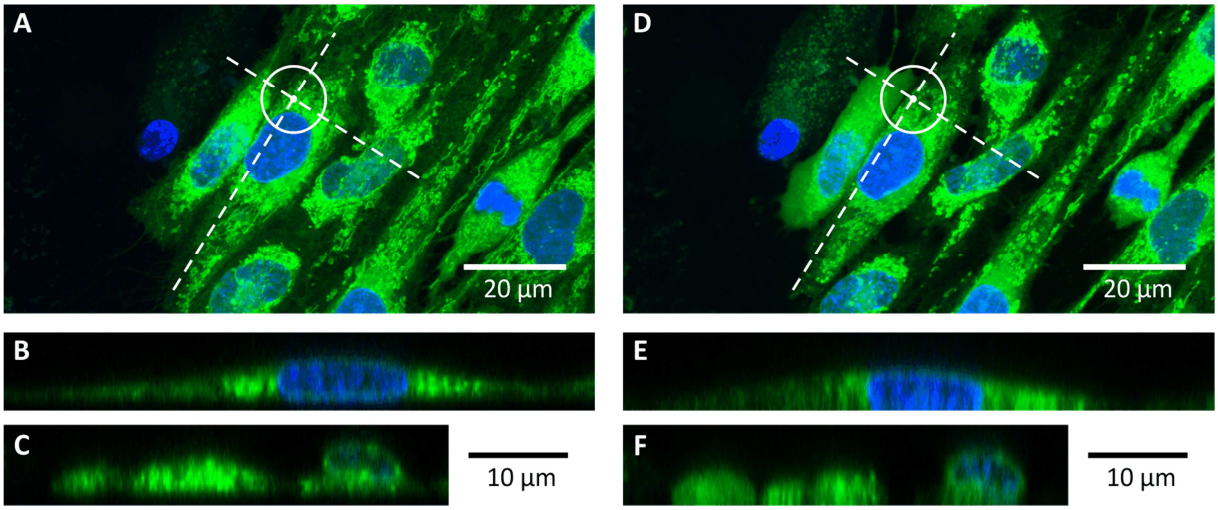

Figure 3.7. Deformation of a cell stimulated next to the nucleus, revealed by fluorescence of DAF-FM T. The fluorophores diffused into the entire volume of the cytosol, filling the bulk of the cell. Images (A) and (D) were acquired before and after pressurization, respectively. The stimulated area is marked with a white circle on both pictures. Cross-sections of the cells were acquired along vertical planes (dashed lines), along the cell axis (B, E) and perpendicular to it (C, F). The images (B) and (E) show a significant displacement of the nucleus (see section 1.1), but no major deformation of the bulk. A slight change in the cross-sectional shape is shown in (C) and (F), yet it is by no means comparable to the deformation of the actin cytoskeleton shown in Figure 3.3. The traces of contact point height and elasticity parameter for the stimulated cell are presented in Figure 3.1 B. Loading of the cells with DAF-FM was not effective in this trial – the dye was compartmentalized, thus the quality of the images deteriorated.

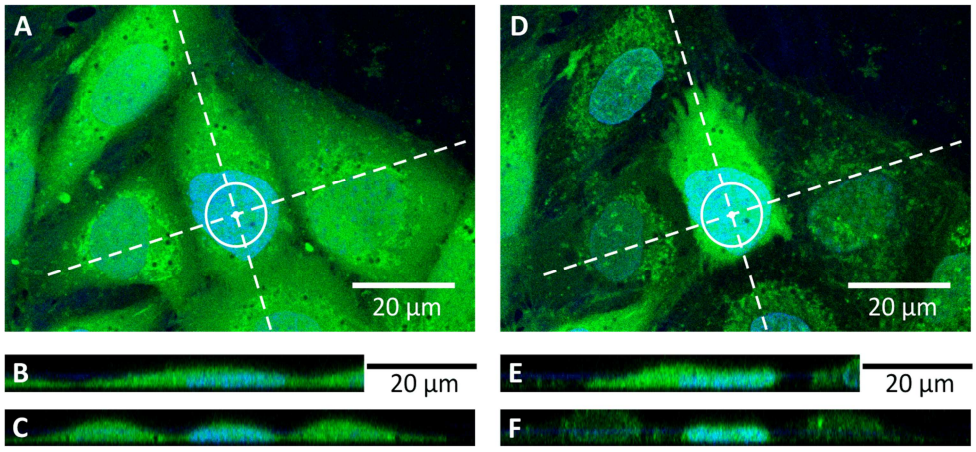

Figure 3.8. Deformation of a cell stimulated right over the nucleus. Like in Figure 3.7, images were acquired before (A, B, C) and after (D, E, F) pressurization, and the bottom panels show the cross-sectional views on the cell along its axis (B, E) and perpendicular to it (C, F). The deformation of the nucleus is clearly visible in images (E) and (F). Concurrently, a thin layer of cytosol between the area of contact and the nucleus is discernible in all cross-sections. The traces of contact point height and elasticity parameter for the stimulated cell are presented in Figure 3.10 B. The pressurized cell lost contact with its neighbors during the experiment, due to apoptosis of the neighbor cells which occurred short before the end of the trial. This influenced substantially the general morphology of the stimulated cell, nevertheless the visualization of the deformed area of indentation remained reliable.

The two presented figures show a substantial displacement (Figure 3.7) and deformation (Figure 3.8) of the cellular components located beneath the membrane, and concurrently no significant damage to the bulk of the cell. In both cases, the records of contact point height show a slight rise of the pressurized area. These observations are analogical to those from section 3.3 (see Figure 3.3), where the stress fibers were severely deformed, and the contact point height increased in time.

3.5 Production of NO

The number of trials involving measurements of NO production was limited, due to technical difficulties. Firstly, the sample moved out of focus (section 2.5.1) – it took several trials to find a method of monitoring the same planar section of the cell during the entire experiment. Evaluation of the same plane was crucial for reliable comparison of total fluorescence intensity over time. Secondly, the loading with DAF-FM was unsuccessful in a few trials: the dye was compartmentalized (Figure 3.7 and Figure 3.9 B), probably due to hampered formation of liposomes around the molecules of DAF-FM DA.

The measurement of NO production relies on the assumption that the total intensity of fluorescence of DAF-FM T is proportional to the amount of NO produced by the cell. For reliable measurements of fluorescence intensity, the stimulated cell was imaged together with its neighbors. Thus, we could tell whether the observed change in fluorescence intensity was specific to the stimulated cell, or uniform for all cells within the field of view. Additionally, a fragment of empty glass surface was imaged every time, to determine the level of background fluorescence. The total intensity of fluorescence was calculated according to the following formula:

[total intensity] =

= [intensity integrated over the selected cell] – [area of the cell] · [mean background fluorescence]

We never observed a selective increase in fluorescence of the individual stimulated cell. The changes in intensity (increase or decrease) were collective for all cells within the field of view (Figure 3.9). This observation may be due to several reasons:

- rapid diffusion of NO produced in the stimulated cell into the neighbor cells (NO is cell-permeant, but DAF-FM T is not),
- low amount of produced NO remained below the threshold of detection,
- a third factor, following from conditions of the measurement, affected all imaged cells concurrently, and caused a pressure-independent change in fluorescence intensity.

All in all, the applied method did not reveal elevated production of NO in the pressurized cell.

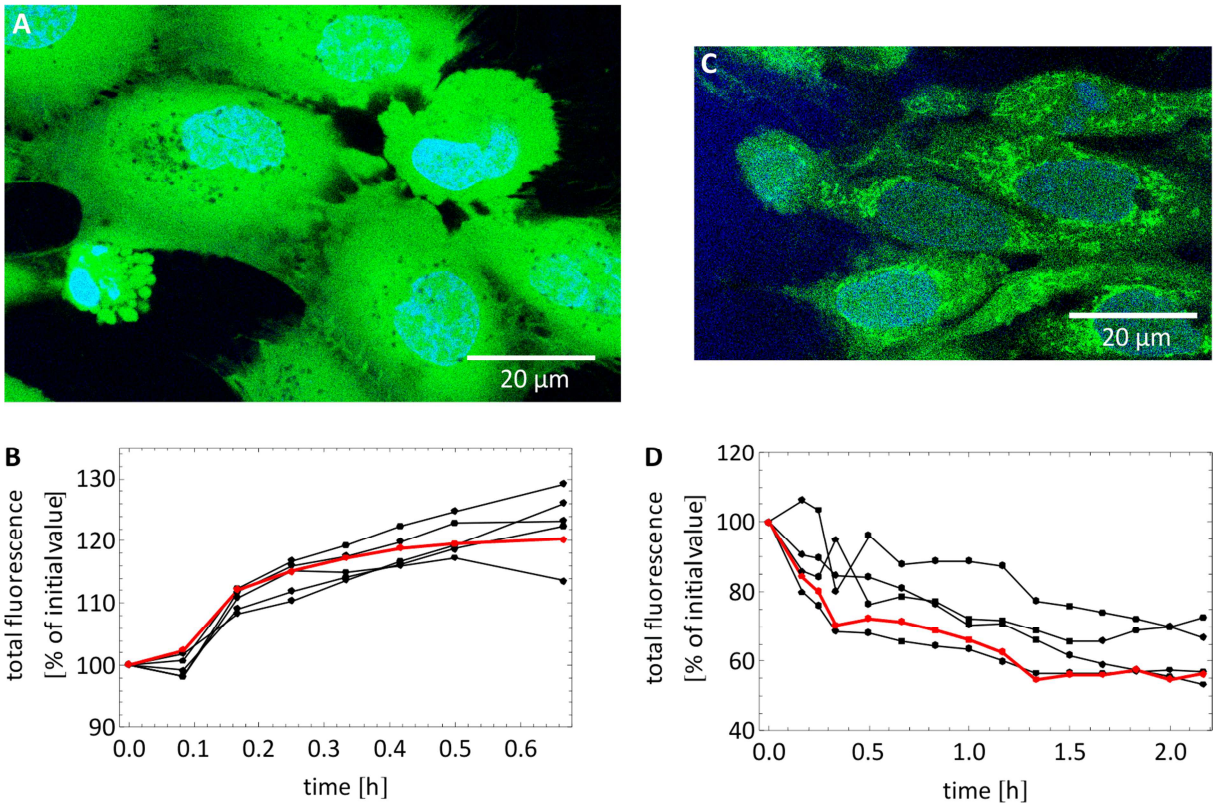

Figure 3.9. Change in intensity of fluorescence of DAF-FM T during application of pulse pressure. Two experiments are reported, in both of them the fluorescence intensity changed uniformly in all cells within the field of view. Image (A) shows the stimulated cell (center-left) with ca. 5 neighbor cells. The graph (B) presents an increase in fluorescence intensity for the pressurized cell (red line) and for other cells (black lines). Similarly, figure (D) shows a decrease in the intensity of fluorescence for the stimulated cell (center of image C), compared to its neighbor cells. The uniform changes in intensity of DAF-FM T fluorescence indicate no measurable difference in NO production between the stimulated cell and the other cells.

3.6 Cells pressurized over the nucleus

In most trials, an endothelial cell was pressurized next to the nucleus (see Figure 3.2). Nevertheless, a few experiments were performed with the probe located right over the nucleus. The response of the cell to such non-standard pressurization (Figure 3.10) was qualitatively similar to the standard reaction reported in section 3.1, but only in terms of contact point height. The records of the elasticity parameter did not show a systematic trend, anyhow comparable to the one presented in Figure 3.1 or Figure 3.13. We presume that the decrease in the elasticity of a region pressurized next to the nucleus follows from structural changes within the cytoskeleton, partly coupled to the nucleus. On the contrary, for pressurization over the nucleus, the dominant probed feature was the nucleus itself, and the impact of the cytoskeleton on the elasticity was less significant – see the disrupted perinuclear actin cap in Figure 3.5.

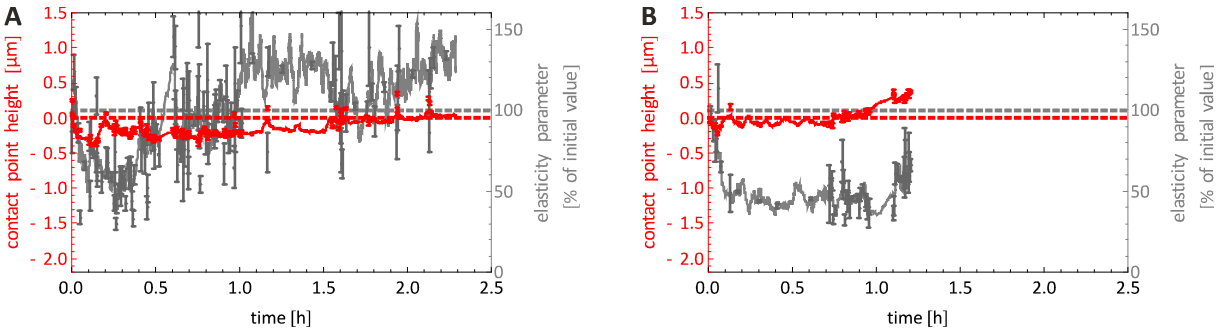

Figure 3.10. Records of contact point height (red) and elasticity parameter (grey) for cells pressurized right over the nucleus (like in Figure 3.8). The systematic rise of the indented area, observed for pressurization next to the nucleus (Figure 3.1), was noted also for cells pressurized over the nucleus. However, no systematic conclusions should be drawn in terms of the elasticity parameter. We believe the measured values of E were substantially influenced by the mechanical properties of the nucleus, which in this case was laying just beneath the cell membrane.

3.7 Experiments with 120/80 mmHg pulse pressure

As a proof of principle, we present the results of a single experiment consisting of pulse pressurization in presence of diastolic pressure, as described in section 2.1.2. We know from other experiments [40] that acute application of large hydrostatic pressure causes stiffening of the endothelial cortex, and the adaptation to the elevated pressure lasts for ca. 1 hour. Therefore, in order to separate the effect of acute application of diastolic pressure from the cell's reaction to pulse pressure, the cells were left under the microscope for 1 hour after elevating the pressure up to 80 mmHg. During that period the cells were imaged with the CLSM every 10 minutes. Then, a given cell was pulse-pressurized for 75 minutes.

The results of the experiment were comparable to the ones obtained for pressurization with 40/0 mmHg waves. The shape of the bulk of the stimulated cell did not change markedly, neither after application of diastolic pressure, nor under pulse pressurization (Figure 3.11). The elasticity parameter measured during the first 30 minutes of application of pulse pressure was significantly higher than the initial value, evaluated before elevation of pressure (Figure 3.12 A). Then, E decreased to the initial level. The extraordinarily high values of elasticity parameter (on the order of 1 kPa) may be interpreted as stiffening of the cells due to application of acute hydrostatic pressure, yet they might have also been caused by a slight misalignment of the cantilever deflection system after elevation of hydrostatic pressure up to 80 mmHg, which was not readjusted afterwards. The record of contact point height did not show any systematic trend. The concentration of NO in the pressurized cell did not change after application of diastolic pressure and pulse pressure (Figure 3.12 B).

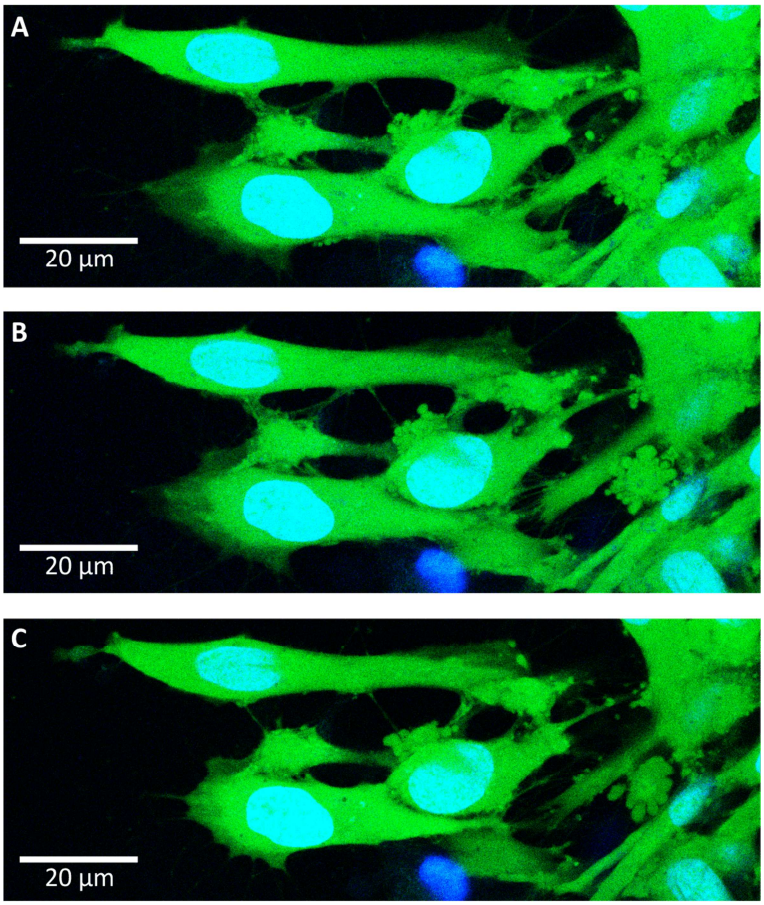

Figure 3.11. Fluorescence images of endothelial cells subjected to acute diastolic pressure of 80 mmHg and pulse pressure waves between 120 mmHg and 80 mmHg. (A) Cells under atmospheric pressure, stained with DAF-FM and Hoechst. (B) Cells after 1 hour of incubation at 80 mmHg. (C) Cells after 50 minutes of local pulse pressurization next to the nucleus of the cell in the bottom-center of the image. The general shape of the bulk did not change after application of diastolic and systolic pressure components. No evident displacement of the nucleus of the stimulated cell was observed.

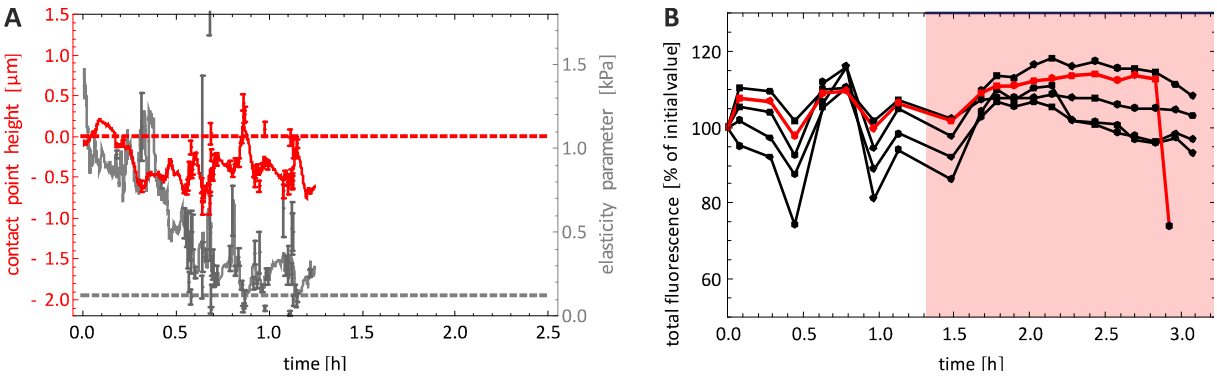

Figure 3.12. (A) Changes in contact point height (red) and elasticity parameter (grey) during pulse pressurization. The value of E measured before elevating the pressure up to 80 mmHg (dashed line) is substantially lower than the values measured at the beginning of pulse pressurization. The 10-fold difference presumably did not result from real stiffening of the cells, due to acute application of high hydrostatic pressure (what of course might have happened), but was an artifact, caused by misalignment of the laser deflection system during elevation of pressure. Nevertheless, the decrease in the elasticity parameter due to pulse pressurization was evident and comparable to the results referred in section 3.1. (B) Intensity of DAF-FM T fluorescence changed uniformly in all cells within the field of view (see Figure 3.11). No systematic trend was observed in fluorescence intensity of the pressurized cell (red line) and other cells (black lines). Hence, no increase in production of NO was detected after application of diastolic pressure and systolic pressure. The period of stimulation with pulse pressure is marked with pink background. The substantial fall of fluorescence intensity of the stimulated cell at the end of the experiment was caused by the apoptosis of the cell and release of the dye into the buffer.

3.8 Experiments without control of the substrate drift

Before joining the AFM setup with the confocal microscope, several experiments were performed, relying only on the records of contact point height and elasticity parameter, supplemented with AFM scans. In many trials we observed the two stage response of contact point height and elasticity (Figure 3.13), just like in later trials presented in section 3.1. However, the total shift in contact point height reached 3 µm which would mean a gigantic growth of cells having a usual height of ca. 6 µm.

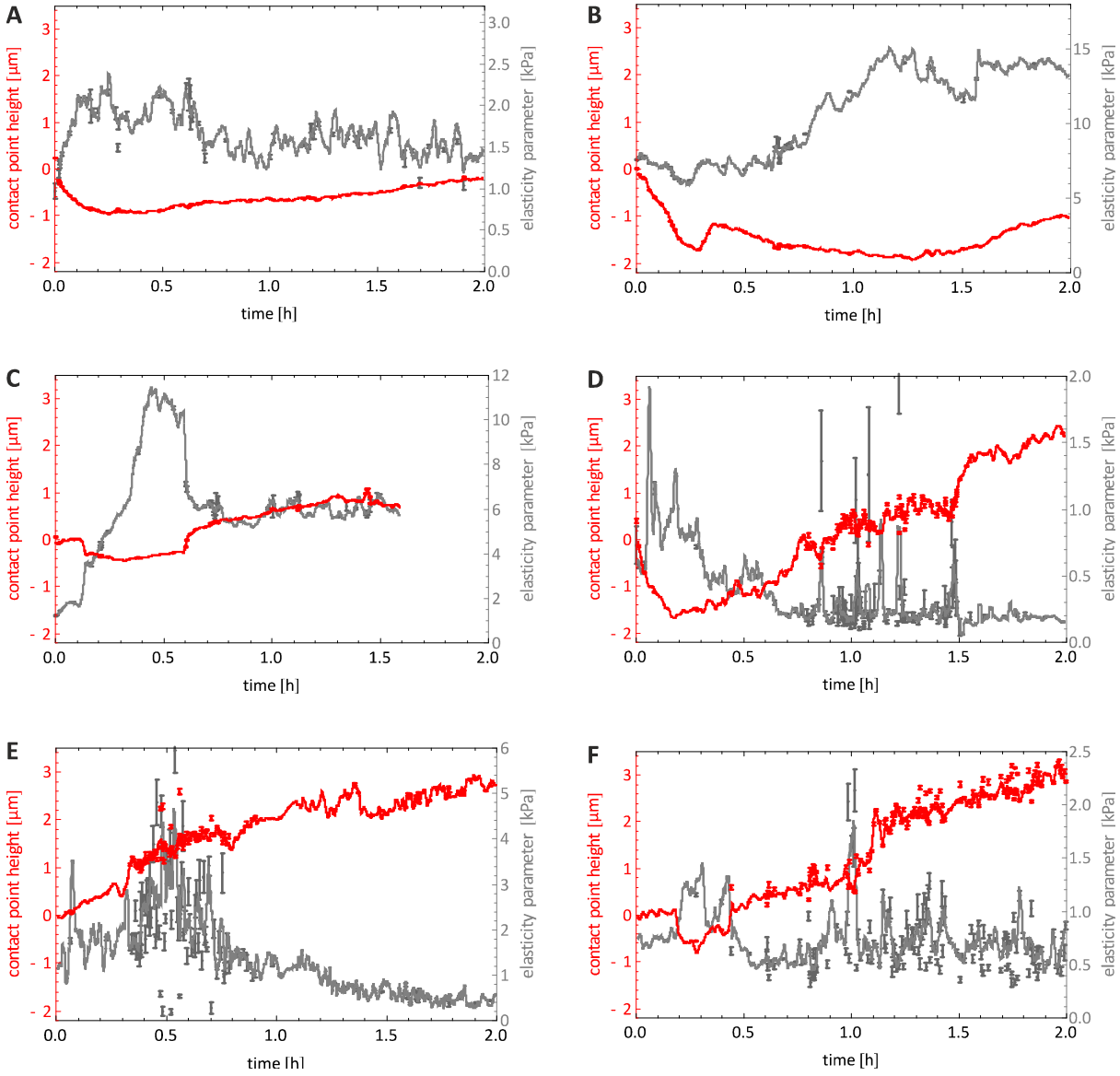

Figure 3.13. Records of contact point height (red) and elasticity parameter (grey), acquired without control of the substrate drift. The general trends were similar to those reported in section 3.1, yet the magnitude of the shift in contact point height reached values as high as 3 µm and was clearly attributable to the artifact (see section 2.5.1). In many graphs one discerns the transient increase in elasticity parameter and the initial downshift of the contact surface, followed by its slow recovery.

In spite of the substrate drift which was unknown and difficult to assess for the presented data, the obtained traces gave us a good intuition for further trials. Indeed, the trends evident on the graphs in Figure 3.13 confirm the general findings reported in section 3.1.

4 CONCLUSIONS

The aims of the reported study were to develop a combined AFM+CLSM setup for local pulse pressurization of endothelial cells, and to investigate the effect of local application of quasi-physiological pulse pressure waves on the nanomechanics and physiology of the endothelium on the level of a single cell. Therefore, the conclusions may be divided into two groups: physiological findings and technical solutions.

4.1 Physiological findings

Local application of pulse pressure on the surface of an aortic endothelial cell does not evoke a whole-cell reaction, and in particular any increase in NO production.

The examined features were cell morphology, arrangement of actin cytoskeleton and production of NO. Although major changes were observed on the pressurized region, the general structure of the actin cytoskeleton of the stimulated cell remained intact. Accordingly [15], no systematic change in production of NO was observed. Collation of those findings with the literature [2] leads to the key conclusion:

No effect of local pressurization on production of NO results either from limited area of stimulation, or from absence of shear stress and circumferential strain.

In the work by Casey et al. [2], NO production was measured under application of all three hemodynamic forces (see section 1.1), including or excluding hydrostatic pressure. Absence of pulsatile hydrostatic pressure attenuated production of NO by a factor of 3.4 ± 1.6. We may understand the conducted experiment as a negative test, answering the question: 'What happens, if the endothelium does not feel pulsatile hydrostatic pressure?'

In this sense, the experiment reported in the thesis was a positive test, answering the question: 'What happens, if the endothelium feels only pulsatile hydrostatic pressure?'. A direct comparison of the results of the two experiments would be inadequate. The two major differences between the experimental setups were absence vs. presence of shear stress and circumferential strain, and local vs. global pressurization of the examined cells. Therefore, the lack of pulse-pressure-induced increase in NO production reported in the thesis must result from one of those differences.

In the study by Casey et al., NO production rate increased under application of pulsatile hydrostatic pressure and shear stress, compared to static culture. Introduction of flow into our experimental setup would allow a direct comparison between local pulse pressurization (our experiment) and

global pulse pressurization (literature). Such comparison would answer the question, whether pressurization of only a part of cell's surface is enough to trigger its response to pulse pressure. This information may be highly valuable with regard to possible (non)existence of the endothelial pressure-sensitive channel.

The network of actin stress fibers is locally deformed/ disrupted by quasi-physiological pressure waves. Concurrently, the nucleus is displaced and deformed.

A mechanistic model of deformable cell features suffices to explain the changes of the cell structure observed in the experiment (Figure 4.1). In the first few minutes of pulse pressurization, the deeply indenting probe exerts a substantial strain on the intact network of stress fibers (Figure 4.1 A, B). Compression of the filamental network, together with its mechanical coupling to the nucleus [38], yields a mechanical resistance of the probed structure, manifested as a transient increase in cortical elasticity parameter (see Figure 3.1 and Figure 3.13). A few hundreds of punches lead to a permanent plastic deformation of the cytoskeleton (Figure 4.1 C), involving displacement and disruption of stress fibers (Figure 3.4 and Figure 3.5), and displacement of the nucleus (Figure 3.2). The deformation of the cytoskeleton explains the initial downshift of the contact area (Figure 3.1 and Figure 3.13). Later on, the cell membrane gradually loses mechanical connections with the cytoskeleton on the surface of contact. An increasing area of the membrane detaches from the deformed cytoskeleton, and the emergent space between the filaments and the membrane is filled with cytosol (Figure 4.1 D). Thus, the membrane is slowly lifted upwards after every punch – this movement is recorded as a gradual increase in contact point height (Figure 3.1). Shortly after the detachment starts, the regime of low indentation into the sample (Figure 2.9 B) no longer corresponds to the cortical network of actin filaments, but to the space filled with cytosol. Therefore, elasticity parameter stabilizes on a low level – the cytosol is far more compliant to elastic deformations than the actin filaments.

The hypothesized model anticipates no substantial deformation of the bulk of the cell after a longer period of pressurization (compare the cell shape in pictures A, D in Figure 4.1). This prediction is confirmed by the three-dimensional confocal images of the stimulated cell acquired before and after application of pulse pressure (see Figure 3.7 and Figure 3.8).

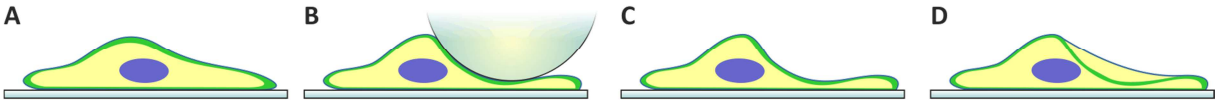

Figure 4.1. The hypothesized mechanistic model explaining the effect of local pressurization on cell structure. An endothelial cell with an intact network of actin filaments (A) is locally stimulated with pulse pressure (B). Subsequent punches deform the cytoskeleton, including the actin stress fibers. The force is transduced to the nucleus, causing its displacement. During the initial period of stimulation a transient increase in elasticity parameter is observed together with a rapid downshift of the pressurized region. These effects are explained by the mechanical compression of the cytoskeleton. After 20-30 minutes, the actin filaments are permanently deformed, creating an invagination on the cell surface (C). Later on, the pulse pressure waves cause a detachment of the cell membrane from the cytoskeleton (D). Thus, the membrane shifts slowly upwards, recovering its height after every punch, and the emergent space is filled with cytosol. This effect is detected as a gradual increase in contact point height, concurrent to stabilization of the elasticity parameter on a low value, corresponding to the great compliance of the cytosol to elastic deformations. The general shape of the cell does not change dramatically due to the stimulation – compare pictures (A) and (D). This finding was confirmed by 3D confocal imaging of cells stained with DAF-FM.

The presented model of cell deformation remains hypothetical, as by now no experiment has been performed, with concurrent control of deformation of the cytoskeleton and the bulk of the cell. Such measurement is not possible using the dyes applied in this study, due to overlapping fluorescence spectra of eGFP and DAF-FM T. We propose an alternative strategy for simultaneous imaging of the cytoskeleton and the bulk (Figure 4.2). Actin filaments should be stained with Lifeact eGFP (see section 2.4.1), whereas instead of imaging the bulk of the cell, we shall visualize its complement. Namely, the buffer filling the fluid chamber should be stained with a cell-impermeant dye whose fluorescence would not overlap with emission from eGFP. For example, dextran functionalized with the fluorophore TRITC emits red fluorescent light and its molecules are too large to penetrate a cell. This approach would enable fine imaging of the boundary of the pressurized cell, not interfering in visualization of the cell organelles. Furthermore, one could quantify the change in cell volume due to pulse pressurization. In order to prove the formulated hypothesis of partial deformation the invagination of the cell membrane, presented in Figure 4.1 C should be captured – this is possible using the proposed technique.

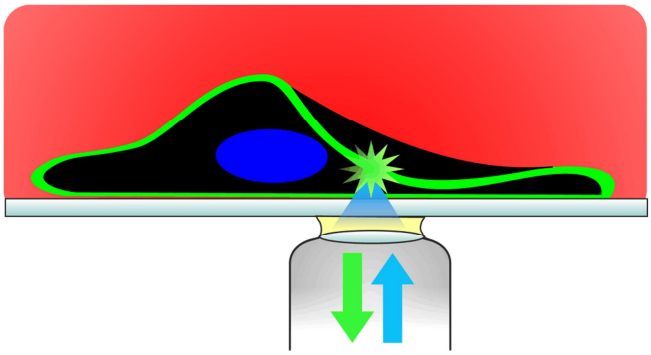

Figure 4.2. Proposed solution for concurrent imaging of the cytoskeletal actin filaments and the boundaries of the cell. Filamental actin should be stained with Lifeact eGFP, and TRITC-functionalized dextran should be dissolved in the buffer filling the fluid chamber. Thus, the complement of the cell's bulk would be imaged, not interfering in visualization of the cell's features. Concurrent imaging of the nucleus, stained with Hoechst) is also possible.

4.2 Technical solutions

We designed and launched a versatile and convenient setup for pressurization and imaging of adherent cells.

The designed setup combines the excellent features of the AFM – accuracy of tip positioning and precision of force measurement – with the advantages of the CLSM, namely the capability of imaging of the cell structure with superb resolution.

Pulse pressure may be applied over a controlled area, with adjustable amplitude and frequency. The constant hydrostatic pressure, simulating the diastolic pressure, may be modified too. Thus, different physiological pressures can be exerted, *e.g.* normal pressure (120/80 mmHg) may be compared to a hypertensive state (160/100 mmHg). Endothelial dysfunction mediates the adverse vascular effects of hypertension [8], particularly in terms of production of NO. Furthermore, low heart rate affects endothelium-dependent vasodilation in hypertension [41]. Hence, we elaborated a versatile method for studying pathophysiological effects.

Various cell lines may be investigated in the designed setup – hence, the response of endothelial cells from different vessels may be compared. Arterial and venous endothelium react differently to cyclic strain and shear stress [4], yet their response to hydrostatic pulse pressure remains to be discovered. The amplitude of pulse pressure is different in arteries and microvessels, hence pressurization should elicit different reactions in various cell types. Other types of adherent cells may also examined: under application of high pulse pressure, smooth muscle cells from the wall of arterioles should contract due to myogenic autoregulation [42].

The setup may be easily adapted to experiments with shear stress and global hydrostatic pulse pressure.

Pulse pressure may be transduced to the cells by manipulating the pressure in the entire fluid chamber. This can be done by introducing an oscillatory movement of the reservoir in the vertical direction, or more conveniently, by substitution of the reservoir with a pump. Thus, the physiological global pressure would be applied to the cells (see Figure 2.3). Hence, the effects of local and global application of hydrostatic pulse pressure could be compared, and contribute to the explanation of pressure sensing in the endothelium.

Introduction of shear stress into the system is expected to elevate the rate of NO production [2]. This can be done by perfusion of the AFM fluid cell, and is possible both in the BioCell, as well as in the custom-built pressure chamber. Such improvement is technically simple, and requires only a simple pump.

It is possible to eliminate or minimize the artifacts hampering the measurements.

Substrate drift, being the most important artifact, can already be controlled and quantified in the current version of the setup (see section 2.5.1). It may be reduced by application of nail polish (see section 2.7.1), yet ideally it should be eliminated. This can be accomplished by supporting the coverslip with a rigid ring, having a central inlet for the objective of the CLSM. Such solution shall reduce the periods of interruption of stimulation, when a fluorescent image/ stack is acquired – coarse refocusing requires at least 10 seconds, and sometimes more than 1 minute is elapsed.

Interference of the AFM laser beam can be avoided by using probes opaque for the laser wavelength (880 nm). Having realized the problem, we tried gluing color dyed polystyrene microspheres (Phosphorex) to cantilevers, expecting extinction of the laser interference. Surprisingly, the artifact sustained. The spheres might not have been totally opaque to the 880 nm light – the manufacturer was not able to provide the absorption spectrum of the dye used for coloring of the microspheres. Nevertheless, the interference can definitely be eliminated.

Autofluorescence of the AFM probe requires stopping the pressurization for a short time, and acquisition of a fluorescence image during that period. Precisely, a Z-stack is acquired every time, to facilitate determination of the position of the focal plane (see section 2.5.1). When the substrate drift is eliminated, one will need to acquire a single frame – this can last as short as 5-10 seconds.

5 PROTOCOLS

5.1 Collagen matrix

Ingredients: 5x RPMI (Sigma Aldrich), 5x HEPES (Sigma Aldrich), 1M NaOH (Calbiochem), laminin (Sigma Aldrich), fibronectin (Roche), collagen IV (Calbiochem).

Prepare the matrix – quantities for coating 6 Ø24 mm coverslips on their centers:

1. Thaw laminin, fibronectin and collagen on ice (this lasts ca. 4 h).
2. Prepare the Ø24 mm coverslips and lay them in 35 mm dishes.
3. Add 30.7 µl of RPMI, 30.7 µl of HEPES and 2.21 µl of NaOH to an Eppendorf tube. Mix the buffer thoroughly. RPMI should change its color to pink due to the change of pH.
4. Add 3.69 µl of laminin, 3.69 µl of fibronectin and 47.2 µl of collagen IV. Mix the solution using the pipette.
5. Place a 17.7 µl droplet of the solution in the middle of each coverslip.
6. Distribute the solution in the middle of each coverslip, so that it forms a circle with a diameter of ca. 11 mm. Immobilize the coverslip by pressing to the bottom of the dish with mini-tweezers.
7. Let the substrates polymerize in the incubator overnight.

On the following day, rinse the coverslips twice with cell culture medium, to wash out the excess NaOH, and seed the cells. Keep in mind that they shall grow faster on coated substrates than on empty coverslips.

5.2 HEPES buffer

Ingredients of the HEPES buffer:

Ingredient	Stock concentration	Final concentration	Quantity per 1000 ml of buffer
NaCl	3 M	140 mM	46.667 ml
KCl	1 M	5 mM	5 ml
$MgCl_2 : 6H_2O$	0.1 M	1 mM	10 ml
$CaCl_2 : 2H_2O$	0.1 M	1 mM	10 ml
glucose	-	5 mM	0.99 g
HEPES	-	10 mM	2.385 g
L-arginine	-	1 mM	0.2107 g

After preparation, the buffer should be filtered.

5.3 Cell culture medium

Ingredient	Producer	Final concentration	Quantity
fetal calf serum	PAA Clone	20%	40 ml
MEM Vitamins	Invitrogen	1%	2 ml
non-essential amino acids	Invitrogen	1%	2 ml
penicillin, streptomycin	Invitrogen	1%	2 ml
minimal essential medium	Invitrogen	-	fill up to 200 ml

All solutions added to the MEM must be filtered to be sterile!

5.4 Cell culture routine

Needed solutions: cell culture medium, PBS^{--} (PAA), trypsin (0.05%, supplemented with 0.02% EDTA, Biochrom).

Cells were sub-cultured 1-2 days after reaching confluence, *i.e.* every 7 days, according to the following procedure:

1. Thaw trypsin and heat it up to 37 ^{o}C together with PBS^{--} and cell culture medium.
2. Remove the medium from the T25 culture flask.
3. Add 7 ml of PBS^{--} and place the flask in the incubator for 1 minute.
4. Remove the PBS^{--} and add 1 ml of trypsin.
5. Place the flask in the incubator for 80 seconds.
6. Check if the cells detached from the bottom of the flask. If not, hit the flask against the desk a few times.
7. Add 9 ml of medium to the flask.
8. Collect the cells suspension with a pipette and add it to a 10 ml Falcon tube.
9. Centrifuge the cells for 5 minutes at 800 rpm.
10. Remove the supernatant.
11. Resuspend the pellet in 2.5 ml of medium.
12. Add 7 ml of medium to a new T25 flask, or 2.5 ml of medium to a 35 mm Petri dish.
13. Suspend an appropriate volume of the cells solution in the medium. The volume depends on the desired dilution and may be calculated according to the following formula: *suspension volume = initial volume / desired dilution · growth surface / initial growth surface* In this case, the initial volume is 2.5 ml. The desired dilution reaches from 2 (cells ready for experiments on the following day) to 50 (cells to be sub-cultured in 7 days). The growth surface is 25 cm^2 for a T25 flask and 9.6 cm^2 for a 35 mm Petri dish. The initial growth surface is 25 cm^2.
14. Place the flask in the incubator.
15. Exchange the medium every 2 days.

5.5 Lifeact transfection

Ingredients: OptiMEM medium (FCS-free, Invitrogen), FuGENE6 transfection reagent (Roche), Lifeact-eGFP plasmid DNA (kind gift from Roland Wedlich-Söldner, MPI Martinsried, Germany).

Prepare the transfection reagent:

1. Mix gently 230 µl of FCS-free OptiMEM medium with 8 µl of FuGENE6.

2. Incubate the solution at room temperature for 5-10 minutes.
3. Add 5 µg of Lifeact-eGFP plasmid DNA.
4. Incubate the solution for 10 minutes at room temperature.

Transfect the cells:

5. Trypsinize and centrifuge cells (like in regular cell culture routine – protocol 1.1).
6. Add OptiMEM medium (with 10% FCS) to cell culture dishes.
7. Resuspend the pellet in OptiMEM (with 10% FCS).
8. Add cell suspension to the transfection reagent (final dilution 1:7) and mix gently.
9. Add the transfection solution to the dishes.
10. Incubate the dishes for 30-40 minutes on a rotatory shaker (180 rpm), in an incubator.
11. Culture cells in an incubator until they reach confluence.
12. After 24 h change the medium to regular cell culture medium.

5.6 Hoechst staining

Ingredients: Hoechst 33342 (Invitrogen), HEPES buffer.

1. Keep the dye in a dark place to prevent photobleaching.
2. Heat HEPES buffer up to 37 ^{o}C.
3. Wash the cells twice with the buffer.
4. Add 1 µl of the Hoechst dye to 990 µl of the buffer.
5. Exchange the buffer from the cells for the dye solution.
6. Place the sample in the incubator (37 ^{o}C) for 30 minutes.
7. Wash the cells twice with the buffer.

Keep the sample in a dark place and proceed with the experiment.

5.7 DAF-FM staining

Ingredients: DAF-FM DA (5 mM solution in DMSO, Sigma Aldrich), Pluronic F 127 (25% solution in DMSO, Merck), HEPES buffer.

Cells should be confluent on the day of the experiment (confluent cells have highest eNOS expression).

1. Keep the dye in a dark place to prevent photobleaching.
2. Heat HEPES buffer and Pluronic up to 37 ^{o}C.
3. Thaw the DAF-FM DA solution.

4. Mix 3 µl of Pluronic with 6 µl of DAF-FM DA. Leave the mixture for a few minutes in a dark place, so that Pluronic liposomes form properly.
5. Wash the cells twice with the buffer.
6. Add 990 µl of the buffer to the solution of DAF-FM DA.
7. Exchange the buffer from the cells for the DAF-FM DA solution.
8. Place the sample in the incubator (37 ^{o}C) for 30 minutes.
9. Wash the cells twice with the buffer.

Keep the sample in a dark place and proceed with the experiment.

6 BIBLIOGRAPHY

1. Sato, M. & Ohashi, T. Biorheological views of endothelial cell responses to mechanical stimuli. *Biorheology* **42**, 421–441 (2005).

2. Casey, P. J. *et al.* The effect of combined arterial hemodynamics on saphenous venous endothelial nitric oxide production. *Journal of Vascular Surgery* **33**, 1199–1205 (2001).

3. Malek, a M. & Izumo, S. Mechanism of endothelial cell shape change and cytoskeletal remodeling in response to fluid shear stress. *Journal of cell science* **109 (Pt 4**, 713–26 (1996).

4. Sung, H.-J., Yee, A., Eskin, S. G. & McIntire, L. V Cyclic strain and motion control produce opposite oxidative responses in two human endothelial cell types. *American journal of physiology. Cell physiology* **293**, C87–94 (2007).

5. Vouyouka, A., Salib, S. & Cala, S. Chronic high pressure potentiates the antiproliferative effect and abolishes contractile phenotypic changes caused by endothelial cells in cocultured smooth muscle. *Journal of Surgical …* **351**, 344–351 (2003).

6. Salwen, S. a, Szarowski, D. H., Turner, J. N. & Bizios, R. Three-dimensional changes of the cytoskeleton of vascular endothelial cells exposed to sustained hydrostatic pressure. *Medical & biological engineering & computing* **36**, 520–7 (1998).

7. Silverthorn, D. U. *Human Physiology. An integrated approach*. (Pearson Education, Inc.: 2010).

8. Landmesser, U. & Drexler, H. Endothelial function and hypertension. *Current opinion in cardiology* **22**, 316–20 (2007).

9. Yang, Z., Venardos, K. & Jones, E. Identification of a novel polymorphism in the 30UTR of the L-arginine transporter gene SLC7A1. Contribution to hypertension and endothelial dysfunction. *Circulation* **115**, 1269–1274 (2007).

10. Safar, M. E. Systolic blood pressure, pulse pressure and arterial stiffness as cardiovascular risk factors. *Curr Opin Nephrol Hypertens* **10**, 257–261 (2001).

11. Asmar, R., Safar, M. E. & Queneau, P. Pulse pressure - An Important Tool in Cardiovascular Pharmacology and Therapeutics. *Drugs* **63**, 927–932 (2003).

12. Folgering, J. H. a *et al.* Molecular basis of the mammalian pressure-sensitive ion channels: focus on vascular mechanotransduction. *Progress in biophysics and molecular biology* **97**, 180–95 (2008).

13. Martinac, B., Buechner, M., Delcour, a H., Adler, J. & Kung, C. Pressure-sensitive ion channel in Escherichia coli. *Proceedings of the National Academy of Sciences of the United States of America* **84**, 2297–301 (1987).

14. Fels, J., Jeggle, P., Kusche-Vihrog, K. & Oberleithner, H. Cortical actin nanodynamics determines nitric oxide release in vascular endothelium. *PloS one* **7**, e41520 (2012).

15. Fels, J., Callies, C., Kusche-Vihrog, K. & Oberleithner, H. Nitric oxide release follows endothelial nanomechanics and not vice versa. *Pflügers Archiv : European journal of physiology* **460**, 915–23 (2010).

16. Ju, H., Zou, R., Venema, V. J. & Venema, R. C. Direct interaction of endothelial nitric-oxide synthase and caveolin-1 inhibits synthase activity. *J Biol Chem* **272**, 18522–18525 (1997).

17. Palmer, R. M., Ferrige, A. G. & Moncada, S. Nitric oxide release accounts for the biological activity of endothelium-derived relaxing factor. *Nature* **327**, 524–526 (1987).

18. Gamboa, A., Shibao, C. & Diedrich, A. Contribution of endothelial nitric oxide to blood pressure in humans. *Hypertension* **49**, 170–177 (2007).

19. Szczygiel, A. M., Brzezinka, G., Targosz-Korecka, M., Chlopicki, S. & Szymonski, M. Elasticity changes anti-correlate with NO production for human endothelial cells stimulated with TNF-α. *Pflügers Archiv : European journal of physiology* **463**, 487–96 (2012).

20. Tojkander, S., Gateva, G. & Lappalainen, P. Actin stress fibers--assembly, dynamics and biological roles. *Journal of cell science* **125**, 1855–64 (2012).

21. Sneddon, I. The relation between load and penetration in the axisymmetric Boussinesq problem for a punch of arbitrary profile. *International Journal of Engineering Science* **3**, 47–57 (1965).

22. Johnson, K. *Contact mechanics*. (Cambridge University Press: 1987).

23. Cappella, B. & Dietler, G. Force-distance curves by atomic force microscopy. *Surface Science Reports* **34**, 1–104 (1999).

24. Heuberger, M., Dietler, G. & Schlapbach, L. Elastic deformations of tip and sample during atomic force microscope measurements. *Journal of Vacuum Science & Technology B: Microelectronics and Nanometer Structures* **14**, 1250–1254 (1996).

25. Carl, P. & Schillers, H. Elasticity measurement of living cells with an atomic force microscope: data acquisition and processing. *Pflügers Archiv : European journal of physiology* **457**, 551–9 (2008).

26. Riedl, J., Crevenna, A. & Kessenbrock, K. Lifeact: a versatile marker to visualize F-actin. *Nature Methods* **5**, 605–608 (2008).

27. Johnson, I. D. The Molecular Probes Handbook: A Guide to Fluorescent Probes and Labeling Technologies. (Life Technologies Corporation: 2010).

28. Kojima, H. *et al.* Fluorescent Indicators for Imaging Nitric Oxide Production. *Angewandte Chemie (International ed. in English)* **38**, 3209–3212 (1999).

29. Itoh, Y. *et al.* Determination and bioimaging method for nitric oxide in biological specimens by diaminofluorescein fluorometry. *Analytical biochemistry* **287**, 203–9 (2000).

30. Hermanowicz, P., Sarna, M., Burda, K. & Gabryś, H. JRobust: a Java Application for Analysis of Force Curves. Unpublished manuscript. Jagiellonian University, Kraków, Poland.

31. Lin, D., Dimitriadis, E. & Horkay, F. Robust strategies for automated AFM force curve analysis-I. Non-adhesive indentation of soft, inhomogeneous materials. *Journal of Biomechanical Engineering* **129**, 430–440 (2007).

32. Lin, D., Dimitriadis, E. & Horkay, F. Robust strategies for automated AFM force curve analysis-II: adhesion-influenced indentation of soft, elastic materials. *Journal of Biomechanical Engineering* **129**, 904–912 (2007).

33. Costa, K. D., Sim, A. J. & Yin, F. C.-P. Non-Hertzian approach to analyzing mechanical properties of endothelial cells probed by atomic force microscopy. *Journal of Biomechanical Engineering* **128**, 176–184 (2006).

34. Hutter, J. L. & Bechhoefer, J. Calibration of atomic-force microscope tips. *Review of Scientific Instruments* **64**, 1868–1873 (1993).

35. Owen, R. & Müller, T. Attaching microspheres to cantilevers using the NanoWizard ® Life Science stage and AFM head Microsphere cantilever tips. *JPK* 1–8

36. Mathur, A. B., Collinsworth, A. M., Reichert, W. M., Kraus, W. E. & Truskey, G. A. Endothelial, cardiac muscle and skeletal muscle exhibit different viscous and elastic properties as determined by atomic force microscopy. *Journal of biomechanics* **34**, 1545–53 (2001).

37. Grinspan, J. B., Mueller, S. N. & Levine, E. M. Bovine endothelial cells transformed in vitro by benzo(a)pyrene. *J. Cell. Physiol.* **114**, 328–338 (1983).

38. Maniotis, a J., Chen, C. S. & Ingber, D. E. Demonstration of mechanical connections between integrins, cytoskeletal filaments, and nucleoplasm that stabilize nuclear structure. *Proceedings of the National Academy of Sciences of the United States of America* **94**, 849–54 (1997).

39. Guolla, L., Bertrand, M., Haase, K. & Pelling, A. E. Force transduction and strain dynamics in actin stress fibres in response to nanonewton forces. *Journal of cell science* **125**, 603–13 (2012).

40. Prystopiuk, V., Oberleithner, H. & Fels, J. Acute pressure-dependent endothelial nanomechanics. Unpublished work. University of Münster, Germany.

41. Maio, R. *et al.* Heart rate affects endothelial function in essential hypertension. *Internal and emergency medicine* **8**, 211–9 (2013).

42. Sun, Z., Martinez-Lemus, L. A., Hill, M. A. & Meininger, G. A. Extracellular matrix-specific focal adhesions in vascular smooth muscle produce mechanically active adhesion sites. *American journal of physiology Cell physiology* **295**, C268–C278 (2008).

Acknowledgement

This study was financially supported by the European fund JCET-UJ No. POIG.01.01.02-00-069/09.